ROYAL SOCIETY OF CHEMISTRY

PAPER

Check for updates

Comparison of secondary organic aerosol generated from the oxidation of laboratory precursors by hydroxyl radicals, chlorine atoms, and bromine atoms in an oxidation flow reactor†

Andrew T. Lambe, [ID] *[a] Anita M. Avery, [ID] [a] Nirvan Bhattacharyya, [ID] [b] Dongyu S. Wang,‡[b] Mrinali Modi,[b] Catherine G. Masoud,[b] Lea Hildebrandt Ruiz [ID] [b] and William H. Brune[c]

The role of hydroxyl radicals (OH) as a daytime oxidant is well established on a global scale. In specific source regions, such as the marine boundary layer and polluted coastal cities, other daytime oxidants, such as chlorine atoms (Cl) and even bromine atoms (Br), may compete with OH for the oxidation of volatile organic compounds (VOCs) and/or enhance the overall oxidation capacity of the atmosphere. However, the number of studies investigating halogen-initiated secondary organic aerosol (SOA) formation is extremely limited, resulting in large uncertainties in these oxidative aging processes. Here, we characterized the chemical composition and yield of laboratory SOA generated in an oxidation flow reactor (OFR) from the OH and Cl oxidation of n-dodecane (n-C_{12}) and toluene, and the OH, Cl, and Br oxidation of isoprene and α-pinene. In the OFR, precursors were oxidized using integrated OH, Cl, and Br exposures ranging from 3.1×10^{10} to 2.3×10^{12}, 6.1×10^{9} to 1.3×10^{12} and 3.2×10^{10} to 9.7×10^{12} molecules cm^{-3} s^{-1}, respectively. Like OH, Cl facilitated multistep SOA oxidative aging over the range of OFR conditions that were studied. In contrast, the extent of Br-initiated SOA oxidative aging was limited. SOA elemental ratios and mass yields obtained in the OFR studies were comparable to those obtained from OH and Cl oxidation of the same precursors in environmental chamber studies. Overall, our results suggest that alkane, aromatic, and terpenoid SOA precursors are characterized by distinct OH- and halogen-initiated SOA yields, and that while Cl may enhance the SOA formation potential in regions influenced by biogenic and anthropogenic emissions, Br may have the opposite effect.

1 Introduction

The atmosphere is an oxidizing environment. Gas-phase oxidants, including ozone (O_3), hydroxyl radicals (OH), nitrate radicals (NO_3), chlorine atoms (Cl), and bromine atoms (Br), can react with organic and inorganic pollutants to generate a myriad of gas- and condensed-phase oxidation products. The importance of each oxidant in different parts of the atmosphere depends on the local meteorology, emissions, and photochemistry. Globally, OH is the most important oxidant: there are many ways to generate it during the daytime from precursors that are widely distributed throughout the atmosphere,

and, unlike O_3, it reacts with most inorganic and organic compounds.[1] With regards to atmospheric aerosols, OH is particularly important in initiating the oxidation of sulfur dioxide (SO_2) to generate sulfuric acid and initiating the oxidation of volatile organic compounds (VOCs) to generate low volatility organic compounds (LVOC) that condense to form secondary organic aerosol (SOA). NO_3 is an important oxidant at nighttime[2] and in some cases during the daytime,[3,4] particularly in source regions influenced by emissions from unsaturated VOCs emitted from plants and wildfires.[5]

Significant Cl production occurs in regions such as the marine boundary layer,[6] polluted coastal cities,[7] and the Arctic atmosphere.[8,9] Most VOCs react with Cl approximately 10 to 100 times faster than their corresponding rate of reaction with OH. Thus, when atmospheric Cl mixing ratios are high enough, Cl may compete with OH in the oxidation of VOCs and/or otherwise enhance the overall oxidation capacity of the atmosphere. Additionally, significant inland Cl production has been observed,[10–12] bleach washing has been shown to initiate significant indoor chlorine chemistry,[13–15] and both Cl and Br

[a]*Aerodyne Research Inc., Billerica, Massachusetts, USA. E-mail: lambe@aerodyne.com*

[b]*The University of Texas at Austin, USA*

[c]*Pennsylvania State University, USA*

† Electronic supplementary information (ESI) available: mercury lamp emission spectra, Cl and Br exposure calibration data, supplemental high-resolution aerosol mass spectra, KinSim mechanism. See https://doi.org/10.1039/d2ea00018k

‡ Present address: Paul Scherrerr Institute, Villagen, Switzerland.

have been linked to enhanced secondary aerosol formation in China.[16] Br contributes to springtime polar mercury and O_3 depletion[9,17,18] reacts with dimethyl sulfide, alkenes, and aldehydes at rates that are similar to their reaction rates with OH, and, like Cl, induces significant multiphase chemistry in organic aerosols.[19–21]

Large environmental chambers have been used for decades to study complex SOA formation chemistry. Multi-instrument, multi-investigator chamber studies have provided comprehensive data sets that transform existing concepts of SOA formation and aging and SOA models.[22] The recent emergence of oxidation flow reactors (OFRs) complements chambers through their lower operation/maintenance costs, portability for *in situ* oxidative aging of ambient and source emissions, and ability to access photochemical aging timescales of up to several days.[23–28] To date, the vast majority of SOA formation studies in chambers and OFRs have used O_3, OH, and to a lesser extent NO_3, to mimic daytime and nighttime oxidation of hydrocarbons. The handful of studies that have measured yields of SOA obtained from Cl oxidation of VOCs have shown that Cl exposure generates SOA in yields that are comparable to, or exceed, OH oxidation of the same precursors.[29–36] SOA formed from Br oxidation of VOCs has not been studied; models including halogen chemistry assume the same yield of SOA is obtained regardless of whether Cl and Br is the initiating oxidant.[16]

To investigate these knowledge gaps, we characterized the chemical composition and yield of laboratory SOA generated in an OFR from the OH, Cl and Br oxidation of a set of anthropogenic and biogenic VOCs. OFRs use residence times that are on the order of minutes and oxidant concentrations that are typically 100–1000 times higher than ambient levels; these factors may make the chemistry and microphysics in the OFR somewhat different from the chemistry and microphysics in the atmosphere.[37,38] Thus, we also compared the chemical composition and mass yields of SOA obtained from OH and Cl oxidation of the same precursors in the OFR with previous chamber studies.

2 Experimental

Experiments were conducted inside a Potential Aerosol Mass (PAM) OFR (Aerodyne Research, Inc.), which is a horizontal 13 L aluminum cylindrical chamber (46 cm long × 22 cm ID) operated in continuous flow mode, with 6.0–6.8 L min^{-1} flow through the reactor.[39] The corresponding calculated mean residence time in the OFR, τ_{OFR}, ranged from 114 to 130 s. An electroconductive Teflon coating was applied to the OFR to improve chemical compatibility with halogen precursors while maintaining high transmission of gases and particles.[40] Two low-pressure mercury (Hg) lamps that were isolated from the sample flow using type 214 quartz sleeves were used to photolyze oxidant precursors. As discussed in Section 2.1 and shown in Fig. S1,† different lamps were used for different OFR methods to maximize the overlap between the absorption cross section of the oxidant precursor and the range of achievable oxidant exposure. A fluorescent dimming ballast (IZT-2S28-D, Advance Transformer Co.) was used to regulate current

applied to the lamps. The UV irradiance was measured using a photodetector (TOCON-GaP6, sglux GmbH) and was varied by changing the control voltage applied to the ballast between 1.5 and 10 VDC. The corresponding actinic flux ranged from approximately 1×10^{14} to 3×10^{15} photons cm^{-2} s^{-1}.[39,41]

2.1 Oxidant generation

2.1.1 OH production and quantification. OH was generated from the combined photolysis of O_2 and H_2O at $\lambda = 185$ nm plus photolysis of O_3 at $\lambda = 254$ nm using two low-pressure germicidal Hg lamps (GPH436T5VH/4P, Light Sources, Inc.); this method is hereafter referred to as "OFR185". Segments of opaque heat shrink tubing were applied to approximately 86% of the illuminated section of the lamps to further reduce the lamp output below what is achievable using the ballast dimming voltage alone.[39] Across all OH-OFR experiments, the relative humidity (RH) was controlled with a Nafion membrane humidifier (Perma Pure) and ranged from 30.9 to 43.3%; corresponding H_2O mixing ratios were between 1.01 to 1.52% at OFR temperatures ranging from 26.2 to 28.8 °C. The integrated OH exposure (OH_{exp}) in the OFR, defined as the product of the mean OH concentration and τ_{OFR}, was calculated using eqn (1) that was developed specifically from OH_{exp} calibration experiments for the GPH436T5VH/4P lamps:[39]

$$\log[OH_{exp}] = (10.098 + (0.15062 - 0.44244 \times OHR_{ext}^{0.18041} + 0.031146 \times \log[O_3 \times OHR_{ext}^{0.1672}]) \times \log[O_3] + \log[H_2O]) + \log\left(\frac{\tau_{OFR}}{124}\right)$$

(1)

where OHR_{ext} (external OH reactivity, s^{-1}) is the product of the SOA precursor mixing ratio and its bimolecular OH rate coefficient (cm^3 $molecules^{-1}$ s^{-1}, hereafter "cm^3 s^{-1}") and $[O_3]$ is the ozone concentration (molecules cm^{-3}, hereafter "cm^{-3}") measured at the exit of the OFR. The estimated uncertainty in calculated OH_{exp} values obtained using eqn (1) was ±50%. Over the range of OFR185 conditions that were used, OH_{exp} values calculated using eqn (1) ranged from 3.1×10^{10} to 2.3×10^{12} molecules cm^{-3} s (hereafter "cm^{-3} s"), or approximately 6 h to 18 d of atmospheric oxidation at $[OH] = 1.5 \times 10^6$ cm^{-3}.[42]

2.1.2 Cl and Br generation and quantification. Cl was generated *via* photolysis of chlorine (Cl_2) at $\lambda = 313$ or 369 nm ($Cl_2 + h\nu \rightarrow 2Cl$) or photolysis of oxalyl chloride ($C_2Cl_2O_2$) at $\lambda = 254$ or 313 nm ($C_2Cl_2O_2 + h\nu \rightarrow 2Cl + 2CO$). $C_2Cl_2O_2$ has been used as a Cl precursor in chamber and flow tube studies;[43–45] here, its usage enabled the investigation of the potential role of unwanted photolysis of Cl-SOA at $\lambda = 254$ nm, a long-standing concern of OH-OFR studies.[46] Similarly, Br was generated *via* photolysis of bromine (Br_2) at $\lambda = 369$ or 421 nm ($Br_2 + h\nu \rightarrow 2Br$) or photolysis of oxalyl bromide ($C_2Br_2O_2$) at $\lambda = 254$ nm. $C_2Br_2O_2$ is less studied than $C_2Cl_2O_2$, but appears to follow a similar photodissociation mechanism as $C_2Cl_2O_2$,[47,48] and so we assume its photolysis proceeds *via* the reaction $C_2Br_2O_2 + h\nu \rightarrow 2Br + 2CO$. These methods are hereafter referred to as "OFR313-iCl_2", "OFR369-iCl_2", "OFR254-i$C_2Cl_2O_2$", "OFR313-i$C_2Cl_2O_2$", "OFR369-iBr_2", "OFR421-iBr_2", and "OFR254-

688 | *Environ. Sci.: Atmos.*, 2022, **2**, 687–701

© 2022 The Author(s). Published by the Royal Society of Chemistry

iC$_2$Br$_2$O$_2$", where applicable ("i" = inject; thus, "iCl$_2$" means Cl$_2$ was the radical precursor injected into the OFR). Fig. S1† shows absorption cross sections for Cl$_2$,[49] Br$_2$,[50] C$_2$Cl$_2$O$_2$,[44] and C$_2$Br$_2$O$_2$,[51,52] as well as emission spectra obtained from the manufacturer for the aforementioned lamp types. Across all Cl-OFR and Br-OFR experiments, the RH ranged from 1.1 to 4.1% at T = 24.2 to 28.0 °C. A compressed gas cylinder containing 0.1% Cl$_2$ in N$_2$ (Praxair) was used to supply Cl$_2$ to the OFR. The Cl$_2$ mixing ratio entering the OFR (1.9–24.7 ppmv) was calculated from the Cl$_2$ mixing ratio in the compressed gas mixture and the dilution ratio of 15–200 cm^3 min^{-1} into 8000 cm^3 min^{-1} carrier gas. C$_2$Cl$_2$O$_2$, C$_2$Br$_2$O$_2$, and Br$_2$ vapor were supplied to the OFR using a sealed permeation tube (EMPTY-HE, VICI) filled with each liquid and placed in a permeation tube oven that was heated to 80–90 °C. A carrier gas flow of 100 cm^3 min^{-1} zero air was used to transfer C$_2$Cl$_2$O$_2$, C$_2$Br$_2$O$_2$, or Br$_2$ vapor from the oven into the OFR. The C$_2$Cl$_2$O$_2$, C$_2$Br$_2$O$_2$, and Br$_2$ mixing ratios (C) entering the OFR were calculated using eqn (2):

$$ C = \frac{P \times 24.47/\text{MW}}{F} \quad (2) $$

where P was the measured permeation rate (1.74 × 10^5, 6.32 × 10^4, 9.68 × 10^4 ng min^{-1}), MW was the molecular weight (126.93, 215.83, or 159.81 g mol^{-1}), and F was the dilution flow rate (8000 cm^3 min^{-1}). Here, the calculated C$_2$Cl$_2$O$_2$, C$_2$Br$_2$O$_2$, and Br$_2$ mixing ratios were 4.2, 1.8, and 1.9 ppmv, respectively.

Integrated Cl and Br exposures (Cl$_{exp}$, Br$_{exp}$) were characterized in offline calibration experiments by measuring the decay of O$_3$ injected into the OFR and measured using an O$_3$ analyzer (2B Technologies) as a function of lamp voltage. O$_3$ concentrations were allowed to stabilize before initiating Cl$_{exp}$ and Br$_{exp}$ measurements, during which steady-state levels of O$_3$ were obtained with the lamps turned off (O$_{3,i}$). Then, the lamps were turned on, and O$_3$ concentrations were allowed to stabilize before being measured at illuminated steady-state conditions (O$_{3,f}$) following reaction with Cl or Br. The Cl or Br exposure (Cl$_{exp}$, Br$_{exp}$) at each condition was calculated using eqn (3) and (4):

$$ \text{Cl}_{exp} = \frac{1}{k_{O_3}^{Cl}} \times -\ln\left(\frac{[O_{3,f}]}{[O_{3,i}]}\right) \quad (3) $$

$$ \text{Br}_{exp} = \frac{1}{k_{O_3}^{Br}} \times -\ln\left(\frac{[O_{3,f}]}{[O_{3,i}]}\right) \quad (4) $$

where $k_{O_3}^{Cl}$ and $k_{O_3}^{Br}$ are the bimolecular Cl + O$_3$ and Br + O$_3$ reaction rate coefficients. Here, we used $k_{O_3}^{Cl}$ = 1.21 × 10^{-11} and $k_{O_3}^{Br}$ = 1.16 × 10^{-12} cm^3 s^{-1}.[53]

Because [Cl$_2$] was varied in experiments that used OFR313-iCl$_2$ and OFR369-iCl$_2$ to generate Cl, separate calibration experiments were performed to measure Cl$_{exp}$ as a function of [Cl$_2$]. To correct for Cl or Br suppression that occurs in the presence of external Cl or Br reactivity (ClR$_{ext}$, BrR$_{ext}$), which is the product of the O$_3$ mixing ratio and its bimolecular Cl or Br rate coefficient, [O$_{3,i}$] was varied from 242 to 3360 ppbv in Cl-OFR calibration experiments and 369 to 7191 ppbv in Br-OFR calibration experiments. These calibration conditions achieved ClR$_{ext}$ values ranging from 72 to 1000 s^{-1} and BrR$_{ext}$ values ranging from 12 to 226 s^{-1}, which approximately span the range of ClR$_{ext}$ and BrR$_{ext}$ values in the OFR conditions listed in Table 1. Example OFR313-iCl$_2$, OFR254-iC$_2$Cl$_2$O$_2$, OFR369-iBr$_2$, OFR254-iC$_2$Br$_2$O$_2$ calibration data are shown in Fig. S2–S5.† Calibration results indicate that Cl$_{exp}$ decreased by a factor of 4 to 12 at each lamp setting over the range of ClR$_{ext}$ values shown in Fig. S2,† with the largest Cl suppression occurring at lower lamp voltage, as expected. Similarly, Br$_{exp}$ decreased by a factor of 2 to 60 using OFR369-iBr$_2$ (Fig. S4†) and by a factor of 2 to 28 using OFR254-iC$_2$Br$_2$O$_2$ (Fig. S5†). Here, we assumed that a specific ClR$_{ext}$ or BrR$_{ext}$ value suppressed Cl$_{exp}$ or Br$_{exp}$ by the same amount regardless of the source of ClR$_{ext}$ or BrR$_{ext}$ (*e.g.* O$_3$ in calibrations, or VOCs in SOA studies). This assumption may have introduced uncertainty in some cases, such as OFR conditions where VOCs were short-lived and their Cl or Br oxidation products had significantly different Cl or Br reaction rates. Because ClO$_x$ and BrO$_x$ chemistry in Cl-OFR and Br-OFR calibration experiments was more complex than the analogous HO$_x$ chemistry in OH-OFR calibration experiments, we assumed ±70% uncertainty in Cl$_{exp}$ and Br$_{exp}$ values.

Table 1 Summary of OFR experimental conditions. OH was generated *via* OFR185, Cl was generated *via* OFR254-iC$_2$Cl$_2$O$_2$, OFR313-iC$_2$Cl$_2$O$_2$, OFR313-iCl$_2$, or OFR369-iC$_2$Cl$_2$O$_2$, and Br was generated *via* OFR254-iC$_2$Br$_2$O$_2$, OFR369-iBr$_2$, or OFR421-iBr$_2$; for details see Section 2.1

VOC/oxidant	[VOC]$_0$ (ppb)	[C$_2$Cl$_2$O$_2$] (ppm)	[Cl$_2$] (ppm)	[C$_2$Br$_2$O$_2$] (ppm)	[Br$_2$] (ppm)	RH (%)	T (°C)	Oxidant exposure (cm^{-3} s)
n-C$_{12}$/OH	21	—	—	—	—	30.9	26.2	2.2 × 10^{11} to 2.1 × 10^{12}
n-C$_{12}$/Cl	21	4.2	—	—	—	1.2	26.1	3.3 × 10^{10} to 2.3 × 10^{11}
Toluene/OH	45	—	—	—	—	31.7	26.2	2.6 × 10^{11} to 2.3 × 10^{12}
Toluene/Cl	45	4.2	—	—	—	1.1	26.9	2.7 × 10^{10} to 4.5 × 10^{11}
Toluene/Cl	45	—	4.9–24.7	—	—	1.2	24.2	2.3 × 10^{10} to 1.3 × 10^{12}
Isoprene/OH	48	—	—	—	—	43.3	27.2	3.1 × 10^{10} to 9.6 × 10^{11}
Isoprene/Cl	48	—	1.9–24.4	—	—	4.0	26.5	6.1 × 10^9 to 2.9 × 10^{11}
Isoprene/Br	144	—	—	1.8	—	4.0	27.8	3.2 × 10^{10} to 2.6 × 10^{12}
α-Pinene/OH	30	—	—	—	—	28.2	28.8	6.7 × 10^{10} to 1.2 × 10^{12}
α-Pinene/Cl	30	4.2	—	—	—	1.4	28.0	3.9 × 10^{10} to 1.2 × 10^{11}
α-Pinene/Br	90	—	—	1.8	—	4.1	25.6	9.8 × 10^{10} to 2.9 × 10^{12}
α-Pinene/Br	90	—	—	—	1.9	3.9	26.0	9.6 × 10^{11} to 9.7 × 10^{12}

A subset of OFR421-iBr$_2$ calibration conditions that were applicable to α-pinene/Br experiments (lamp voltages higher than 4 V and/or BrR$_{ext}$ < 90 s^{-1}) depleted all the O$_3$ that was injected into the OFR. To constrain Br$_{exp}$ at these conditions, we compared Br$_{exp}$ obtained using OFR421-iBr$_2$ and OFR369-iBr$_2$ at otherwise identical OFR conditions when Br$_{exp}$ < 3 × 10^{12} cm^{-3} s using both methods. Br$_{exp}$ obtained using OFR421-iBr$_2$ was approximately 2.16 times higher than Br$_{exp}$ obtained using OFR369-iBr$_2$ (Fig. S6†), which is consistent with a higher Br$_2$ absorption cross section at λ = 421 nm than at λ = 369 nm.[50] Br$_{exp}$ values obtained at the other OFR369-iBr$_2$ conditions were then multiplied by 2.16 to obtain Br$_{exp}$ values at OFR421-iBr$_2$ conditions with equivalent lamp settings and BrR$_{ext}$ values.

Calculated Cl$_{exp}$ values in SOA experiments ranged from 6.1 × 10^9 to 1.3 × 10^{12} cm^{-3} s, or approximately 1.2 d to 8.2 months of atmospheric oxidation at [Cl] = 6 × 10^4 cm^{-3}.[18] Similarly, calculated Br$_{exp}$ values ranged from 3.2 × 10^{10} to 9.7 × 10^{12} cm^{-3} s, or approximately 1 h to 16 d at [Br] = 7 × 10^6 cm^{-3}.[18] These simple calculations should be interpreted as a rough estimate of the photochemical age in a representative source region with active Cl or Br photochemistry (e.g., Arctic spring), and may vary by orders of magnitude elsewhere.

2.2 Photochemical model

To investigate the fate of O$_3$ in our Cl$_{exp}$ and Br$_{exp}$ calibration experiments, and to build a foundation for characterizing the concentrations of inorganic halogens generated in the OFR, we developed a photochemical box model that was implemented in the KinSim chemical kinetic solver.[54] The KinSim mechanism shown in Table S1† contains 66 reactions to model HO$_x$ concentrations in OFRs[39,55,56] plus 139 reactions that were added to model concentrations of Cl$_2$, C$_2$Cl$_2$O$_2$, Br$_2$, C$_2$Br$_2$O$_2$, Cl, ClO, ClO$_2$, ClO$_3$, OClOO, ClOO, Cl$_2$O, Cl$_2$O$_2$, HCl, HOCl, Cl$_2$O$_3$, Br, BrO, BrO$_2$, HBr, HOBr, and BrCl. Inputs to the KinSim model were [O$_3$] (242 to 7191 ppb), UV flux (3.5 × 10^{13} to 3.5 × 10^{15} photons cm^{-2} s^{-1}), RH = 1%, T = 25 °C, and τ$_{OFR}$ = 130 s (modeled as plug flow). Over this range of OFR conditions, the model suggests that >97% of reactive O$_3$ loss was due to reaction with Cl across all OFR313-iCl$_2$, OFR369-iCl$_2$, OFR254-iC$_2$Cl$_2$O$_2$, and OFR313-iC$_2$Cl$_2$O$_2$ calibration conditions, with the remaining O$_3$ lost to reaction with ClO. Similarly, we estimate that >99% of reactive O$_3$ loss was due to reaction with Br across all OFR369-iBr$_2$, OFR421-iBr$_2$, OFR254-and iC$_2$Br$_2$O$_2$ calibration conditions, with the remaining O$_3$ lost to reaction with BrO. We estimate that Cl or Br regeneration via photolysis of ClO$_x$ and BrO$_x$ biased calibrated Cl$_{exp}$ or Br$_{exp}$ values by <2% or <14% respectively. Because we already applied ±70% uncertainty estimates to Cl$_{exp}$ and Br$_{exp}$ values, we did not apply additional correction factors to the calibration data.
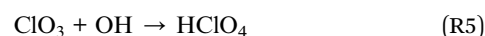
2.3 Particle generation
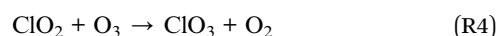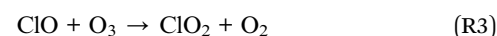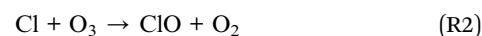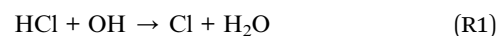
SOA particles were generated via gas-phase OH or Cl oxidation of n-dodecane (n-C$_{12}$) or toluene, or OH, Cl, or Br oxidation of isoprene or α-pinene, followed by homogeneous nucleation; we hereafter refer to SOA formation initiated by OH, Cl, and Br as "OH-SOA", "Cl-SOA" or "Br-SOA" respectively. These precursors were chosen to cover a range of surrogate anthropogenic and biogenic compounds that enabled comparison with results from Cl-initiated chamber SOA formation studies.[29–33,35,36] Particle number concentrations and mobility size distributions were measured with a TSI scanning mobility particle sizer (SMPS), and ensemble aerosol mass spectra were measured with an Aerodyne long high-resolution time-of-flight aerosol mass spectrometer (L-ToF-AMS). Liquid solutions containing the precursor diluted to 10% (v/v) in carbon tetrachloride were injected into the OFR carrier gas flow at liquid flow rates (Q$_{VOC,l}$) ranging from 0.94 to 2.8 μL h^{-1} using a syringe pump. The VOC mixing ratio entering the OFR, r$_{VOC,g}$, was calculated using the ideal gas law as applied by Liu et al.[57] in eqn (5):

$$r_{VOC,g} \ (ppb) = \frac{Q_{VOC,l}}{Q_{carrier}} \times \frac{\rho}{MW} \times \frac{RT}{P} \times r_{VOC,L} \times \frac{10^7}{60} \quad (5)$$

where ρ (g cm^{-3}) and MW (g mol^{-1}) are the liquid density and molecular weight, R (8.314 J mol^{-1} K^{-1}) is the universal gas constant, T (K) is temperature, P (hPa) is pressure, r$_{VOC,l}$ is the VOC mixing ratio in solution, and 10^7 is a lumped pressure, volume, density and time unit conversion factor. Calculated r$_{VOC,g}$ values for n-C$_{12}$, toluene, isoprene and α-pinene are listed in Table 1. For isoprene and α-pinene Br-SOA experiments, we used r$_{VOC,g}$ values that were 3 times higher than in corresponding OH-SOA and Cl-SOA experiments in order to promote homogenous nucleation of Br-SOA.

Over the course of our studies, we learned that conditioning the OFR with humidified carrier gas containing O$_3$ and OH while transitioning from Cl-SOA to OH-SOA studies generated >100 μg m^{-3} and >10^7 cm^{-3} of homogenously nucleated particles that gradually subsided over hours to days. As shown in Fig. S7,† L-ToF-AMS spectra of these particles contained chlorinated ion signals (and their primary Cl isotope at m/z +2), at m/z = 35 (Cl$^+$), 36 (HCl$^+$), 51 (ClO$^+$), 67 (ClO$_2^+$), 70 (Cl$_2^+$), 83 (ClO$_3^+$), and 100 (HClO$_4^+$), suggesting that these particles contained perchloric acid (HClO$_4$) and/or perchlorate salts.[58,59] Significant signal at m/z = 44 (CO$_2^+$) was also observed and is a known artifact from the interaction of inorganic salts on surfaces inside the AMS.[60] During these transient conditioning periods, we hypothesize that perchlorate was generated from the reaction of O$_3$ with aqueous HCl on the walls of the OFR[61] and/or in the gas phase from the reactions:[62]

$$HCl + OH \rightarrow Cl + H_2O \quad (R1)$$

$$Cl + O_3 \rightarrow ClO + O_2 \quad (R2)$$

$$ClO + O_3 \rightarrow ClO_2 + O_2 \quad (R3)$$

$$ClO_2 + O_3 \rightarrow ClO_3 + O_2 \quad (R4)$$

$$ClO_3 + OH \rightarrow HClO_4 \quad (R5)$$

To minimize the influence of perchlorate on ensuing OH-SOA measurements, the OFR was conditioned with O$_3$ and OH until ClO$_x^+$ signals in the AMS returned to background levels.

2.4 Analysis

2.4.1 L-ToF-AMS. L-ToF-AMS spectra were analyzed using ToF-AMS analysis software,[63] which yielded high-resolution mass spectra, hydrogen-to-carbon (H/C) and oxygen-to-carbon (O/C) ratios, and abundances of the default $C_xH_y^+$, $C_xH_yO^+$, and $C_xH_yO_{>1}^+$ ion groups. We created additional $C_xH_yClO_z^+$ (including Cl^+ and HCl^+) and $C_xH_yBrO_z^+$ (including Br^+ and HBr^+) ion groups to distinguish ions containing Cl or Br atoms. Elemental analysis was performed using the methods of Aiken *et al.*[64] to enable direct comparison with chamber SOA measurements[30,65,66] that were published prior to more recent methods proposed by Canagaratna *et al.*[67]

To compare our measurements with chamber Cl-SOA mass spectra obtained with an Aerodyne quadrupole aerosol chemical speciation monitor (Q-ACSM) with unit mass resolution,[32,33,35,36] corresponding O/C ratios for those data were calculated using the equation O/C = $3.82 \times f_{44} + 0.0794$,[64] where f_{44} was the fraction of Cl-SOA signal at $m/z = 44$. We used L-ToF-AMS data to confirm the literature O/C-f_{44} parameterization was accurate for Cl-SOA generated in the OFR in this study. However, H/C ratios of Cl-SOA calculated using the equation H/C = $1.01 + 6.07 \times f_{43} - 16.01 \times f_{43}^2$,[68] where f_{43} was the fraction of Cl-SOA signal at $m/z = 43$, were systematically $\approx 20–40\%$ higher than H/C ratios calculated from the L-ToF-AMS spectra (Fig. S8†). Additionally, significant contributions to $m/z = 43$ from both $C_3H_7^+$ and $C_2H_3O^+$ ions in n-C_{12} Cl-SOA spectra complicated application of the H/C-f_{43} correlation proposed by Ng *et al.*[68] Thus, we developed a different parameterization to calculate the H/C ratio of Cl-SOA from the fraction of L-ToF-AMS signal at $m/z = 41$, which contained one alkyl ion ($C_3H_5^+$). We then applied the equation H/C = $5.032 \times f_{41}^{0.1485} - 1.737$ (Fig. S9†) to calculate the H/C ratio of chamber-generated n-C_{12}, isoprene, and α-pinene Cl-SOA obtained with the Q-ACSM. For chamber-generated toluene Cl-SOA data published in Dhulipala *et al.*,[35] because only f_{43} was available, we calculated $f_{41} : f_{43} = 0.17$ in our toluene Cl-SOA spectra, used this result to estimate f_{41} for their toluene chamber Cl-SOA spectra, and then calculated H/C ratio using the equation described above.

2.5 SOA yields

SOA mass yields were calculated from the ratio of SOA mass formed to precursor gas reacted. The SOA mass was calculated from the integrated SMPS particle volume and the SOA particle density, ρ_{SOA}, which was calculated using eqn (6):[69]

$$\rho = \frac{12 + H/C + 16 \times O/C}{7 + 5 \times H/C + 4.15 \times O/C} \qquad (6)$$

We estimated the fraction of precursor gas reacted from the product of the OH_{exp}, Cl_{exp}, or Br_{exp} and the bimolecular rate coefficients of n-C_{12} + OH/Cl, toluene + OH/Cl, isoprene + OH/Cl/Br, and α-pinene + OH/Cl/Br.[70–76] These calculations suggested that 95–100% of n-C_{12}, 75–100% of toluene, 91–100% of isoprene, and 89–100% of α-pinene reacted across the OFR conditions summarized in Table 1.

SOA yields were corrected for size-dependent particle wall losses in the OFR by applying the particle transmission

efficiency measurements of Bhattarai *et al.*[77] to the SMPS volume-weighted mobility size distributions. Here, the particle wall loss correction factors ranged from 1.07 to 1.38 for mean volume-weighted particle mobility diameters ranging from 180 nm to 36 nm. To investigate the influence of vapor wall losses on SOA yields, we used the LVOC fate correction model,[78,79] which calculates the timescales of diffusional wall losses, gas-phase oxidative loss, and condensation onto aerosols at a user-specified condensation loss rate, OH/Cl/Br exposure and reaction rate coefficient, and OFR residence time values. We assumed that LVOCs had the same OH, Cl, or Br reaction rate coefficients as their VOC precursors. The condensation sink was calculated using the integrated SMPS number-weighted mobility size distributions and assuming a LVOC diffusion coefficient of 0.07 cm² s⁻¹, mean molecular speed of 2×10^4 cm s⁻¹, and mass accommodation coefficient of unity.[78,80,81] In these experiments, mean fractional LVOC wall losses for each precursor/oxidant combination ranged from 0.003 ± 0.001 (n-C_{12}/Cl) to 0.079 ± 0.076 (α-pinene/Br). Thus, we assumed LVOC wall losses were negligible compared to gas-phase oxidative loss and condensation onto aerosols,[82,83] and did not modify SOA yield values to account for them.

3 Results & discussion

3.1 Sample anthropogenic OH-SOA and Cl-SOA mass spectra

Fig. 1 shows L-ToF-AMS spectra of SOA generated from the OH and Cl oxidation of n-C_{12} and toluene. To compare results obtained at lower oxidant exposures that were most applicable to
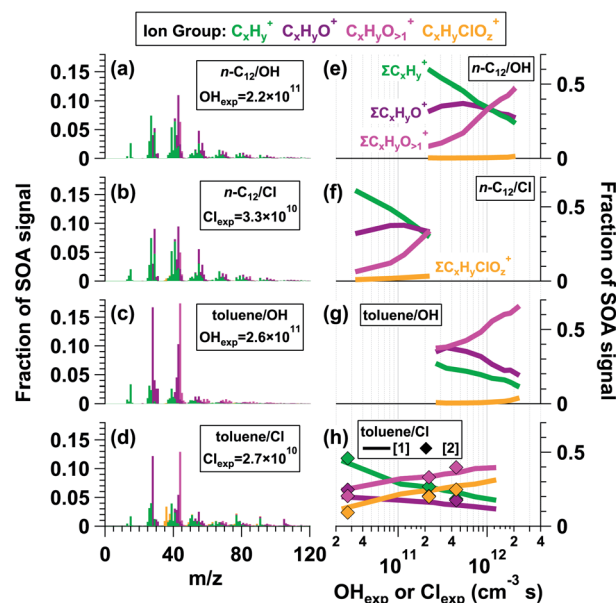

Fig. 1 L-ToF-AMS spectra of SOA generated from the (a and e) OH oxidation of n-C_{12}, (b and f) Cl oxidation of n-C_{12}, (c and g) OH oxidation of toluene, and (d and h) Cl oxidation of toluene. OH_{exp} and Cl_{exp} values listed in (a)–(d) are in units of cm⁻³ s. The toluene Cl-SOA spectrum presented in (d) was generated using OFR254-iC₂Cl₂O₂. Additional notes regarding (h): toluene Cl-SOA was generated using (1) OFR313/369-iCl₂ or (2) OFR254-iC₂Cl₂O₂.

urban atmospheres, the spectra shown were obtained at the lowest OH_{exp} and Cl_{exp} values at which particle formation was observed: $OH_{exp} = 2.2 \times 10^{11}$ and $Cl_{exp} = 3.3 \times 10^{10}$ cm^{-3} s for n-C_{12} OH- and Cl-SOA, and $OH_{exp} = 2.6 \times 10^{11}$ and $Cl_{exp} = 2.7 \times 10^{10}$ cm^{-3} s for toluene OH- and Cl-SOA. For both n-C_{12} OH-SOA and Cl-SOA, the spectra were dominated by $C_xH_y^+$ (green) and $C_xH_yO_1^+$ (purple) ion groups, which contributed ~60% and 31% of the total OH- and Cl-SOA signal, respectively (Fig. 1e and f). Some of the most abundant ions within these groups included signals at $m/z = 27$ ($C_2H_3^+$), 29 (CHO^+), 41 ($C_3H_5^+$), 43 ($C_2H_3O^+ + C_3H_7^+$), and 55 ($C_3H_5O^+ + C_4H_7^+$). Additional signals were present at $m/z = 44$ (CO_2^+), a marker for organic acids in the AMS,[84] and at multiple ion clusters above $m/z = 60$ that contained $C_xH_y^+$, $C_xH_yO_1^+$, and $C_xH_yO_{>1}^+$ (pink) ions.

To characterize the similarity between SOA mass spectra obtained from OH and Cl oxidation of the same precursor, using simple linear regression, we calculated the square of the Pearson correlation coefficient (r^2) between the n-C_{12} OH- and Cl-SOA mass spectra shown in Fig. 1a and b, and between toluene OH- and Cl-SOA mass spectra shown in Fig. 1c and d. OH and Cl oxidation of n-C_{12} generated SOA with similar AMS spectra ($r^2 = 0.94$) because both OH and Cl oxidation of n-C_{12} proceeded *via* hydrogen atom abstraction. In contrast, toluene OH-SOA and Cl-SOA spectra were more distinct from each other: while an r^2 value of 0.87 was obtained between the two spectra, r^2 decreased to 0.57 when contributions from signals at $m/z = 44$ and $m/z = 28$ (CO^+, set equal to CO_2^+ by default) were removed from the regression analysis. Notably, toluene Cl-SOA contained enhanced signals at $m/z = 77$ ($C_6H_5^+$), 91 ($C_7H_7^+$), and 105 ($C_7H_5O^+$) relative to toluene OH-SOA. While the Cl_{exp} used to generate Fig. 1d was 10 times lower than the OH_{exp} used to generate Fig. 1c, toluene reacts with Cl ten times faster than OH;[75] thus, to first order, the extent of OH and Cl oxidation was similar in both cases. The most likely explanation is that Cl oxidation of toluene generated a higher yield of ring-retaining C_6 and C_7 oxidation products because Cl preferentially abstracts H-atoms from the methyl group.[30]

To compare the similarity of n-C_{12} and toluene OH-/Cl-SOA spectra across the range of OH_{exp} or Cl_{exp} values shown in Fig. 1e–h, Fig. S10† plots r^2 values between L-ToF-AMS spectra shown in Fig. 1a or c and n-C_{12} or toluene OH-/Cl-SOA spectra obtained at other OH_{exp} and Cl_{exp}. For example, the r^2 value between Fig. 1a and more-oxidized n-C_{12} OH-SOA spectra decreased from 0.98 to 0.31 with increasing OH_{exp}. For n-C_{12} Cl-SOA, r^2 decreased from 0.94 to 0.43 with increasing Cl_{exp}. Likewise, r^2 between Fig. 1c and more-oxidized toluene OH-SOA spectra decreased from 0.98 to 0.85 with increasing OH_{exp}, and r^2 between Fig. 1c and toluene Cl-SOA spectra decreased from 0.87 to 0.71 with increasing Cl_{exp}.

Fig. 1e, f and g, h plot the fractional contributions of the $C_xH_y^+$, $C_xH_yO_1^+$, $C_xH_yO_{>1}^+$, and $C_xH_yClO_z^+$ ion groups ($f_{C_xH_y^+}$, $f_{C_xH_yO_1^+}$, $f_{C_xH_yO_{>1}^+}$, and $f_{C_xH_yClO_z^+}$) (pale orange) present in n-C_{12} and toluene OH-/Cl-SOA as a function of OH_{exp} and Cl_{exp}. Minimum and maximum fractions of each ion group are provided in Table 2, and the corresponding range of OH_{exp} and Cl_{exp} values are listed in Table 1. Minor contributions from the C_xH_y-ClO_z^+ ion group (orange) to the toluene OH-SOA spectra in Fig. 1g were observed, primarily from signals at Cl^+ and HCl^+. These signals may be associated with NH_4Cl generated from the reaction of trace NH_3 in the system with residual HCl from Cl-OFR studies. While $f_{C_xH_y^+}$ and $f_{C_xH_yO_1^+}$ values spanned similar ranges, the maximum $f_{C_xH_yO_{>1}^+}$ value was lower in n-C_{12} Cl-SOA (0.34) than in n-C_{12} OH-SOA (0.48). For both n-C_{12} OH-SOA and Cl-SOA, $f_{C_xH_y^+}$ decreased monotonically, $f_{C_xH_yO_1^+}$ increased and then decreased, and $f_{C_xH_yO_{>1}^+}$ and $f_{C_xH_yClO_z^+}$ increased monotonically as a function of OH_{exp} and/or Cl_{exp}. Because n-C_{12} has no double bonds for direct Cl addition, one possible source of particulate organic chlorides (ROCl) may have been Cl oxidation of unsaturated dihydrofuran intermediates.[33] Another possible ROCl source involves the reaction $RO_2 + Cl \rightarrow RO + ClO$ followed by the reaction $RO_2 + ClO \rightarrow ROCl + O_2$,[85,86] where RO_2 represents organic peroxy radicals derived from Cl oxidation of n-C_{12} and/or its oxidation products and RO represents alkoxy radicals.

Qualitatively similar changes in toluene OH-SOA and Cl-SOA spectra were observed as a function of OH_{exp} and Cl_{exp}. Because toluene is more volatile than n-C_{12}, addition of more oxygen-containing functional groups was required to generate

Table 2 Summary of OFR experimental results. The fraction of SOA signals detected in $C_xH_y^+$, $C_xH_yO^+$, $C_xH_yO_{\geq1}^+$, $C_xH_yClO_z^+$, and $C_xH_yBrO_z^+$ ion groups ($f_{C_xH_y^+}$, $f_{C_xH_yO^+}$, $f_{C_xH_yO_{>1}^+}$, $f_{C_xH_yClO_z^+}$, and $f_{C_xH_yBrO_z^+}$), oxygen-to-carbon (O/C) and hydrogen-to-carbon (H/C) ratios were obtained from high-resolution analysis of L-ToF-AMS spectra over the range of oxidant exposures summarized in Table 1. SOA yields were calculated as described in Section 2.3

VOC/oxidant	$f_{C_xH_y^+}$	$f_{C_xH_yO^+}$	$f_{C_xH_yO_{>1}^+}$	$f_{C_xH_yClO_z^+}$	$f_{C_xH_yBrO_z^+}$	O/C	H/C	C_{SOA} (µg m^{-3})	Y_{SOA}
n-C_{12}/OH	0.24–0.60	0.30–0.37	0.08–0.48	—	—	0.27–1.05	0.89–1.24	25–132	0.18–0.91
n-C_{12}/Cl	0.30–0.61	0.32–0.37	0.06–0.34	0.009–0.033	—	0.22–0.82	1.20–1.63	160–357	1.1–2.5
Toluene/OH	0.11–0.27	0.19–0.38	0.37–0.66	—	—	0.83–1.51	0.89–1.24	16–93	0.098–0.56
Toluene/Cl	0.18–0.46	0.17–0.25	0.20–0.40	0.09–0.25	—	0.46–1.08	0.86–1.22	24–106	0.15–0.64
Toluene/Cl	0.18–0.44	0.12–0.20	0.24–0.40	0.12–0.31	—	0.53–1.02	0.82–1.07	14–99	0.083–0.58
Isoprene/OH	0.24–0.43	0.37–0.50	0.08–0.38	—	—	0.36–0.91	1.17–1.50	4–53	0.031–0.40
Isoprene/Cl	0.36–0.60	0.30–0.34	0.06–0.17	0.042–0.065	—	0.24–0.55	1.22–1.38	1–29	0.011–0.21
Isoprene/Br	0.46	0.34–0.35	0.05–0.07	—	0.12–0.13	0.29–0.31	1.40–1.44	2–7	0.007–0.018
α-Pinene/OH	0.28–0.46	0.26–0.40	0.13–0.42	—	—	0.38–0.93	1.16–1.48	18–52	0.11–0.31
α-Pinene/Cl	0.29–0.45	0.28–0.34	0.16–0.33	0.058–0.095	—	0.42–0.80	1.18–1.39	37–77	0.22–0.47
α-Pinene/Br	0.49–0.56	0.31–0.32	0.08–0.12	—	0.042–0.063	0.26–0.34	1.36–1.39	0.5–18	0.0006–0.037
α-Pinene/Br	0.55–0.59	0.25–0.26	0.09–0.12	—	0.056–0.063	0.24–0.30	1.33–1.38	1–9	0.003–0.018

condensable oxidation products, resulting in lower initial f_{CxHy^+} and f_{CxHyO1^+} values, with a monotonic decrease in f_{CxHyO1^+} instead of an increase and then decrease as was observed in n-C_{12} SOA. Additionally, higher $f_{CxHyO>1^+}$ values were measured in toluene OH-/Cl-SOA, and higher $f_{CxHyClOz^+}$ values were observed in toluene Cl-SOA than in n-C_{12} SOA. Notably, for Cl-SOA generated from toluene (and, to a lesser extent, n-C_{12}), $f_{CxHyClOz^+}$ followed the same trend as $f_{CxHyO>1^+}$. This suggests that this ion group was also associated with later-generation oxidation products. Because direct Cl addition to the aromatic ring is a minor pathway (*e.g.* Cai *et al.*[30]), ROCl in toluene Cl-SOA may have been generated from RO_2 + ClO reactions, as was hypothesized earlier for ROCl observed in n-C_{12} Cl-SOA. Overall, these observations were consistent with multigenerational oxidative aging of n-C_{12} and toluene OH- and Cl-SOA, where early-generation oxidation products that contributed to the less-oxidized $C_xH_y^+$ and $C_xH_yO_1^+$ ion groups were converted to later-generation oxidation products that contributed to the $C_xH_yO_{>1}^+$ ion groups.

3.2 Sample biogenic OH-SOA, Cl-SOA, and Br-SOA mass spectra

Fig. 2a–f shows L-ToF-AMS spectra of SOA generated from the OH, Cl, and Br oxidation of isoprene and α-pinene. The isoprene OH-SOA, Cl-SOA and Br-SOA mass spectra were obtained at OH_{exp}, Cl_{exp}, and Br_{exp} values of 3.1×10^{10}, 6.1×10^9, and 3.2×10^{10} cm^{-3} s, and the α-pinene OH-SOA, Cl-SOA, and Br-SOA spectra were obtained at OH_{exp}, Cl_{exp}, and Br_{exp} values of

6.8×10^{10}, 3.9×10^{10}, and 5.9×10^{11} cm^{-3} s. All SOA spectra were dominated by signals at $m/z = 29$ (CHO$^+$), 39 ($C_3H_3^+$), 43 ($C_2H_3O^+$), 44 (CO_2^+), and 55 ($C_3H_5O^+$). Thus, at the lower OH, Cl, and Br exposures used to generate Fig. 2 spectra, the main differences were associated with $C_xH_yClO_z^+$ and $C_xH_yBrO_z^+$ ions present in Cl-SOA and Br-SOA.

As was done in Section 3.1, to characterize the similarity of SOA mass spectra obtained from OH, Cl, and Br oxidation of the same precursor, we calculated r^2 values between the isoprene OH-/Cl-/Br-SOA spectra shown in Fig. 2a–c, and between the α-pinene OH-/Cl-/Br-SOA shown in Fig. 2d–f. The r^2 values between isoprene OH-/Cl-SOA and OH-/Br-SOA were 0.83 and 0.93 respectively. Likewise, r^2 values between α-pinene OH-/Cl-SOA and OH-/Br-SOA were 0.86 and 0.92. In each of these cases, removing contributions from $m/z = 43$ or $m/z = 44$ from the regression analysis resulted in a minimal change in r^2. To compare the similarity of isoprene and α-pinene OH-SOA, Cl-SOA and Br-SOA spectra across the full range of experimental conditions that were used, Fig. S11† plots r^2 values between the L-ToF-AMS spectra shown in Fig. 2a and d and corresponding isoprene or α-pinene OH-/Cl-/Br-SOA spectra obtained at other OH_{exp}, Cl_{exp}, and Br_{exp}. The r^2 value between Fig. 2a and more-oxidized isoprene OH-SOA spectra decreased from 0.99 to 0.32 with increasing OH_{exp}. For isoprene Cl-SOA, r^2 increased from 0.83 to 0.87 before decreasing to 0.63 at higher Cl_{exp}, whereas $r^2 = 0.91$–0.92 as a function of Br_{exp} for isoprene Br-SOA. The r^2 value between Fig. 2d and more-oxidized α-pinene OH-SOA spectra decreased from 0.96 to 0.46 with increasing OH_{exp}.
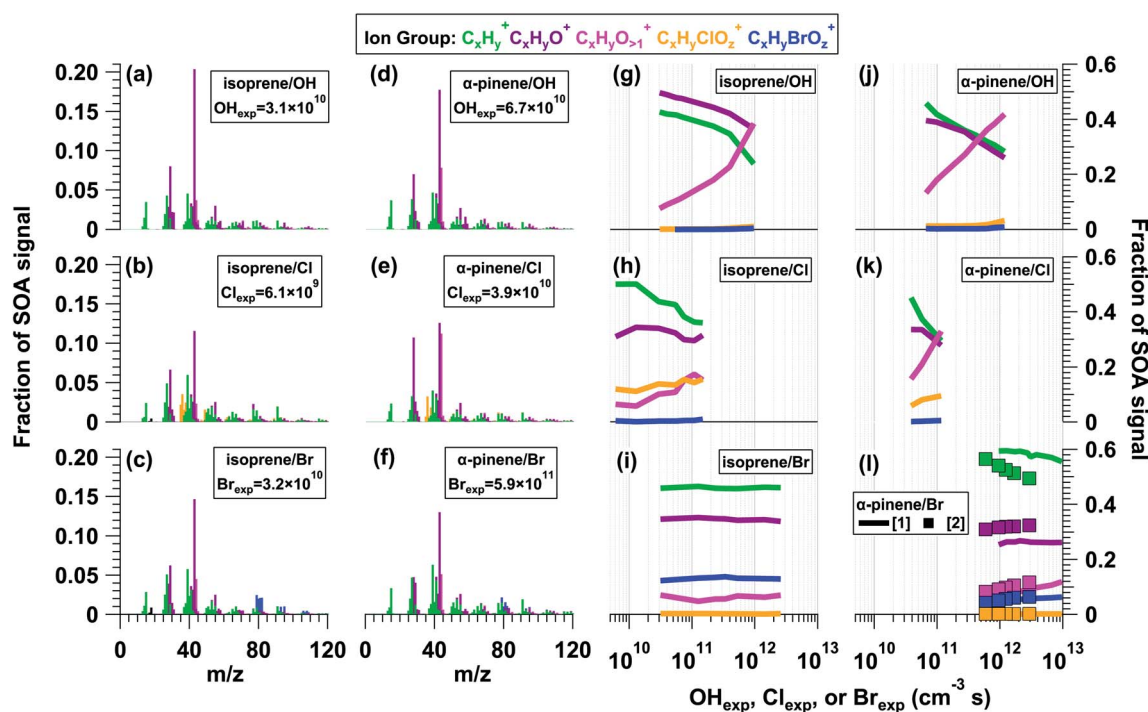

Fig. 2 L-ToF-AMS spectra of SOA generated from the (a and g) OH oxidation of isoprene, (b and h) Cl oxidation of isoprene, (c and i) Br oxidation of isoprene, (d and j) OH oxidation of α-pinene, (e and k) Cl oxidation of α-pinene, and (f and l) Br oxidation of α-pinene. OH_{exp}, Cl_{exp}, and Br_{exp} values listed in (a)–(f) are in units of cm^{-3} s. The α-pinene Br-SOA spectrum presented in (f) was generated using OFR254-iC$_2$Br$_2$O$_2$. Additional figure notes regarding (l): α-pinene Br-SOA was generated using (1) OFR369/421-iBr$_2$ or (2) OFR254-iC$_2$Br$_2$O$_2$.

© 2022 The Author(s). Published by the Royal Society of Chemistry

Environ. Sci.: Atmos., 2022, **2**, 687–701 | **693**

For α-pinene Cl-SOA, r^2 decreased from 0.86 to 0.57, and for α-pinene Br-SOA, r^2 ranged from 0.92–0.93 (OFR254-i$C_2Br_2O_2$) or 0.83–0.86 (OFR369/421-iBr_2) as a function of Br_{exp}.

Fig. 2g–l plot f_{CxHy^+}, f_{CxHyO1^+}, $f_{CxHyO>1^+}$, $f_{CxHyClOz^+}$, and $f_{CxHyBrOz^+}$ (blue) present in isoprene and α-pinene OH-/Cl-/Br-SOA as a function of oxidant exposure. Here, as was observed in Fig. 1g, minor contributions from the $C_xH_yClO_z^+$ ion group (orange) to the α-pinene OH-SOA spectra in Fig. 2g were mostly Cl^+ and HCl^+, and may be associated with NH_4Cl generated from incidental $NH_3 + HCl$ reactions. For isoprene and α-pinene OH-/Cl-SOA, as with toluene OH-/Cl-SOA, f_{CxHy^+} and f_{CxHyO1^+} decreased, and $f_{CxHyO>1^+}$ and $f_{CxHyClOz^+}$ increased with increasing OH_{exp} or Cl_{exp} (Table 2). Despite a similar decrease in f_{CxHy^+} of isoprene OH-SOA and Cl-SOA, the decrease in f_{CxHyO1^+} and increase in $f_{CxHyO>1^+}$ were smaller in isoprene Cl-SOA than in isoprene OH-SOA. This was probably because a higher oxidation state was achieved for isoprene OH-SOA than for isoprene Cl-SOA: the maximum OH_{exp} (9.6×10^{11} cm^{-3} s) was 6.5 times higher than the maximum Cl_{exp} (1.5×10^{11} cm^{-3} s) shown in Fig. 2h, but the isoprene + Cl reaction rate is only 4.3 times faster than the isoprene + OH reaction rate. Due to Cl-induced fragmentation at high Cl_{exp}, the yield and size of isoprene SOA particles generated at $Cl_{exp} = 2.9 \times 10^{11}$ cm^{-3} s were too small for efficient transmission through the L-ToF-AMS inlet.

On the other hand, changes in isoprene and α-pinene Br-SOA composition were minor by comparison. For isoprene Br-SOA, f_{CxHy^+} was approximately constant, f_{CxHyO^+} decreased by less than 0.01, and $f_{CxHyO>1^+}$ and $f_{CxHyBrOz^+}$ increased slightly. For α-pinene Br-SOA, f_{CxHy^+} decreased slightly, while f_{CxHyO1^+}, $f_{CxHyO>1^+}$, and $f_{CxHyBrOz^+}$ increased slightly. Following direct Br addition to α-pinene, additional organic bromide (ROBr)

formation may have occurred *via* $RO_2 + Br$ and/or $RO_2 + BrO$ reactions.[87,88] At a specific Br_{exp}, α-pinene Br-SOA had lower f_{CxHyO^+} and higher f_{CxHyO1^+} when generated *via* OFR254-i$C_2Br_2O_2$ (lines) compared to OFR369/421-iBr_2 (symbols). We do not think that α-pinene Br-SOA photolysis at λ = 254 nm was important when using OFR254-i$C_2Br_2O_2$ (Section 3.5), but other potential reasons for these Br-SOA compositional differences are unclear. Overall, based on these results, we hypothesize that multigenerational oxidative aging of Br-SOA was less extensive than in OH-SOA and Cl-SOA because Br is a more selective oxidant. While OH and Cl are likely reactive towards the majority of early-generation isoprene and α-pinene oxidation products, Br is only known to react efficiently with alkenes and aldehydes, with reactivity towards alcohols, ketones, and peroxides that is orders of magnitude slower than OH or Cl (*e.g.* Manion *et al.*[89]). This hypothesis and its implications will be explored further in Sections 3.4 and 3.5.

3.3 Cl-SOA and Br-SOA mass spectral markers

Fig. 3 shows L-ToF-AMS spectra of $C_xH_yClO_z^+$ ions present in the n-C_{12}, toluene, isoprene and α-pinene Cl-SOA spectra plotted in Fig. 1b, d and 2b, e. The y-axis in Fig. 3a (n-C_{12} Cl-SOA) was multiplied by a factor of 10 to put it on the same scale as Fig. 3b–d. The $f_{C_xH_yClO_z^+}$ was lowest for n-C_{12} Cl-SOA (0.0083) because Cl oxidation proceeded practically exclusively *via* H-abstraction, and was highest for isoprene Cl-SOA (0.114) because Cl oxidation proceeded mostly *via* addition to double bonds. Intermediate $f_{C_xH_yO_zCl^+}$ values of 0.077 and 0.063 were observed for toluene and α-pinene SOA, respectively. Overall, signals at $m/z = 35$ (Cl^+) and $m/z = 36$ (HCl^+) and their isotopes contributed 66 to 81% of the
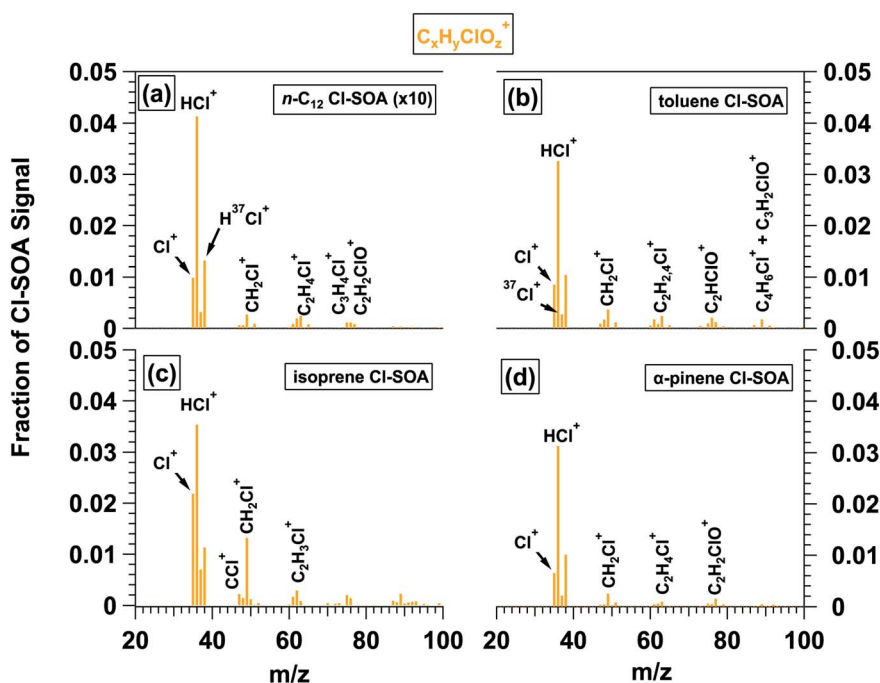

Fig. 3 $C_xH_yClO_z^+$ ions present in L-ToF-AMS spectra of (a) n-C_{12}, (b) toluene, (c) isoprene, and (d) α-pinene Cl-SOA displayed in Fig. 1b, d and 2b, e. The y-axis scale in (a) is multiplied by 10 to put it on the same scale as (b)–(d).

Table 3 Comparison of OFR (this work) and chamber Cl–SOA (all other references listed in table) experimental conditions and results; "N/S" = not specified. O/C and H/C ratios of chamber Cl–SOA were calculated as described in Sect. 2.3. In chamber Cl–SOA studies, the fraction of AMS or ACSM signals contributed by HCl^+ (f_{HCl^+}) was calculated from signals at $m/z = 36 + 38$

VOC	Cl_{exp} (cm^{-3} s)	O/C	H/C	f_{HCl^+}	C_{SOA} (µg m^{-3})	Y_{SOA}	Reference
n-C$_{12}$	3.3×10^{10} to 2.3×10^{11}	0.22–0.82	1.63–1.20	0.006–0.020	160–357	1.1–2.5	This work
n-C$_{12}$	9.8×10^{10} to 1.3×10^{11}	0.32–0.88	1.50–1.26	0.006–0.014	99–149	1.10–1.65	Wang and Hildebrandt Ruiz[33]
Toluene	2.3×10^{10} to 1.3×10^{12}	0.53–1.02	1.07–0.82	0.067–0.159	14–99	0.083–0.58	This work
Toluene	3.3×10^{10} to 2.3×10^{11}	0.46–1.08	1.22–0.86	0.050–0.127	24–106	0.15–0.64	This work
Toluene	N/S	0.69–0.81	0.94–0.89	0.050–0.069	53–136	0.33–0.67	Dhulipala et al.[35]
Toluene	N/S	0.65	1.31	0.071	3–12	0.030–0.079	Cai et al.[30]
Isoprene	6.1×10^{9} to 2.9×10^{11}	0.24–0.55	1.38–1.22	0.042–0.065	1–29	0.011–0.21	This work
Isoprene	N/S	0.45–0.72	1.32–1.11	0.033–0.067	9–80	0.08–0.29	Wang and Hildebrandt Ruiz[32]
α-Pinene	3.9×10^{10} to 1.2×10^{11}	0.42–0.80	1.39–1.18	0.040–0.065	37–77	0.22–0.47	This work
α-Pinene	1.9×10^{11}	0.46–0.65	1.25	0.013–0.056	14–247	0.44–0.96	Masoud and Hildebrandt Ruiz[36]
α-Pinene	N/S	N/S	N/S	N/S	0.0013–176	3.7×10^{-5} to 0.62	Ofner et al.[31]
α-Pinene	N/S	N/S	N/S	N/S	8–33	0.079–0.22	Cai and Griffin[29]

$C_xH_yClO_z^+$ signal across all Cl–SOA types. Other ions that were detected in multiple Cl–SOA spectra included $m/z = 49$ (CH_2Cl^+), 61–63 ($C_2H_{2-4}Cl^+$), 76 (C_2HClO^+) and 77 ($C_2H_2ClO^+$), albeit usually at much lower levels than Cl^+ and HCl^+.

To compare these results with chamber Cl–SOA studies that reported f_{HCl^+} values, Table 3 lists minimum and maximum f_{HCl^+} values measured in OFR- and chamber-generated Cl–SOA at their corresponding Cl_{exp} values. In OFR-generated SOA, as expected, f_{HCl^+} increased as a function of Cl_{exp} in a similar manner to the $C_xH_yClO_z^+$ ion signals shown in Fig. 1f, h and 2h, k. The most significant absolute change in f_{HCl^+} was observed for OFR-generated toluene Cl–SOA, where f_{HCl^+} increased from 0.050 to 0.16 as Cl_{exp} increased from 1.5×10^{10} to 1.3×10^{12} cm^{-3} s. By comparison, f_{HCl^+} measured in chamber-generated toluene Cl–SOA ranged from 0.051 to 0.069.[35] For the other Cl–SOA types, f_{HCl^+} increased from 0.0059 to 0.020 (n-C$_{12}$), 0.046 to 0.071 (isoprene), and 0.041 to 0.065 (α-pinene), respectively. Chamber-generated Cl–SOA had f_{HCl^+} values ranging from 0.008 to 0.014 (n-C$_{12}$), 0.034 to 0.067 (isoprene), and 0.013 to 0.056 (α-pinene).[32,33,36]

L-ToF-AMS spectra of Br–SOA contained a series of $C_xH_yBrO_z^+$ ions (Fig. 4), with $f_{CxHyBrOz^+} = 0.115$ and 0.039 for isoprene and α-pinene Br–SOA, respectively. Because Br oxidation proceeded *via* double-bond addition, $f_{CxHyBrOz^+}$ was higher in isoprene Br–SOA. Signals at $m/z = 79$ (Br^+) and 80 (HBr^+) and their isotopes contributed 58 and 68% of the $C_xH_yBrO_z^+$ signal for isoprene and α-pinene Br–SOA; f_{HBr^+} ranged from 0.035 to 0.042 and from 0.016 to 0.022 for isoprene and α-pinene Br–SOA (Table 3). Analogous to the usage of HCl^+ as a marker ion for ROCl in the AMS,[32] we hypothesize that $H^{79}Br^+$ and/or $H^{81}Br^+$ may be used as simple markers for ROBr in the absence of inorganic halides such as NH_4Br. Depending on the source region, $H^{81}Br^+$ may be easier to resolve than $H^{79}Br^+$ due to sulfate (SO_3^+) interference at $m/z = 79$. Other signals that were detected in both isoprene and α-pinene Br–SOA spectra included $m/z = 93$ and 95 (CH_2Br^+), 106 and 108 ($C_2H_3Br^+$), 121 and 123 ($C_2H_2BrO^+$) and 133 and 135 through 138 ($C_3H_{5-6}BrO^+$). Larger $C_xH_yBrO_z^+$-containing ions up to $m/z = 245$ and 247 were identified in α-pinene Br–SOA (Fig. S12–S13;†

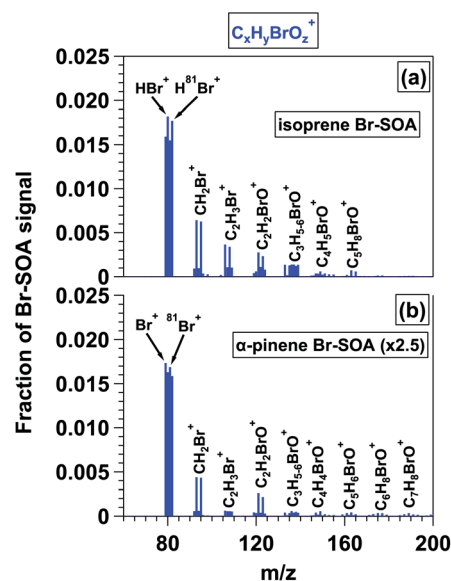**Fig. 4** $C_xH_yBrO_z^+$ ions present in L-ToF-AMS spectra of (a) isoprene and (b) α-pinene Br–SOA displayed in Fig. 2c and f. The y-axis scale in (b) is multipled by 2.5 to put it on the same scale as (a).

both m/z values shown to indicate similar concentrations of $C_{10}H_{14}BrO_2^+$ and its ^{81}Br-containing isotope).

3.4 H/C and O/C ratios of OH–SOA, Cl–SOA and Br–SOA

Van Krevelen diagrams that show H/C ratio as a function of O/C ratio have been used to provide information about the nature of SOA formation and oxidative aging.[90] Typically, with oxidative aging the O/C ratio increases and H/C ratio of SOA decreases as oxygen-containing functional groups are added to a carbon backbone. Here, we use Van Krevelen diagrams to compare the elemental ratios of OH–SOA, Cl–SOA, and Br–SOA discussed in the previous sections. Where applicable, data from chamber SOA studies are included for comparison.

Fig. 5a–d show that chamber- and OFR-generated OH–SOA generally have similar Van Krevelen plots within the limited range of overlap of O/C and H/C values. Chamber-generated n-
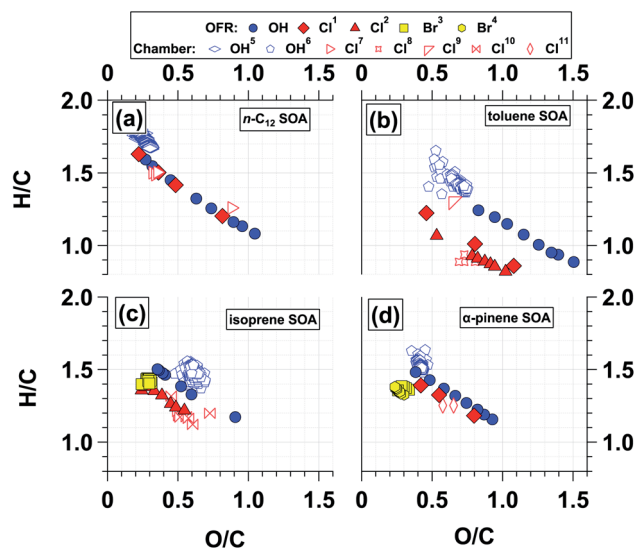
© 2022 The Author(s). Published by the Royal Society of Chemistry

Environ. Sci.: Atmos., 2022, **2**, 687–701 | **695**

Fig. 5 Van Krevelen diagrams showing H/C ratio as a function of O/C ratio for SOA generated from (a) OH and Cl oxidation of n-C$_{12}$, (b) OH and Cl oxidation of toluene, (c) OH, Cl, and Br oxidation of isoprene, and (d) OH, Cl, and Br oxidation of α-pinene. Additional figure notes for superscripts: [1]Cl generated using OFR254/313-iC$_2$Cl$_2$O$_2$; [2]Cl generated using OFR313/369-iCl$_2$; [3]Br generated using OFR254-iC$_2$Br$_2$O$_2$; [4]Br generated using OFR369/421-iBr$_2$; [5]Yee *et al.*;[66] [6]Chhabra *et al.*;[65] [7]Wang and Hildebrandt Ruiz;[33] [8]Dhulipala *et al.*;[35] [9]Cai *et al.*;[30] [10]Wang and Hildebrandt Ruiz;[32] [11]Masoud and Hildebrandt Ruiz.[36]

C$_{12}$ OH-SOA had O/C and H/C values ranging from 0.18 to 0.30 and 1.83 to 1.67, respectively,[66] and OFR-generated n-C$_{12}$ OH-SOA had O/C and H/C values ranging from 0.27 to 1.05 and 1.59 to 1.08. Thus, SOA elemental ratios agree within approximately 5–10% for the most-oxidized chamber-generated n-C$_{12}$ OH-SOA and the least-oxidized OFR-generated n-C$_{12}$ OH-SOA. Similar trends were observed with the other OH-SOA types studied in this work (Fig. 5b–d). Whereas chamber studies have limited ability to generate highly oxidized OH-SOA, here, it was possible to compare H/C and O/C ratios of chamber- and OFR-generated Cl-SOA over a wide range of SOA oxidation state. Chamber-generated n-C$_{12}$ Cl-SOA had O/C and H/C ratios ranging from 0.30 to 0.88 and 1.50 to 1.26 respectively[33] compared to O/C and H/C ratios ranging from 0.22 to 0.82 and 1.63 to 1.20 for OFR-generated n-C$_{12}$ Cl-SOA. At O/C = 0.36, n-C$_{12}$ Cl-SOA H/C ratios agreed within ~1% for chamber and OFR-generated Cl-SOA; likewise, at O/C = 0.82, the H/C ratios agreed within ~5%. These results suggest that Cl-SOA elemental composition is the same regardless of whether it is generated at lower oxidant concentrations over longer exposure times in chambers, or higher oxidant concentrations over shorter exposures times in OFRs, similar to OH-SOA.[91,92]

Fig. 5 also provides insight into differences between OH-, Cl-, and Br-SOA oxidative aging pathways. For systems where H-atom abstraction was the dominant reaction pathway (*e.g.*, n-C$_{12}$), the OH- and Cl-SOA Van Krevelen plots were essentially identical within the range of overlapping H/C and O/C ratios. On the other hand, the H/C ratio of toluene Cl-SOA was consistently ~25–30% lower than the H/C ratio of toluene OH-

SOA at a specific O/C ratio. For example, at O/C ≈ 0.8, H/C = 1.24 for toluene OH-SOA and 1.01 for toluene Cl-SOA. Because the Van Krevelen slopes (Δ(H/C)/Δ(O/C)) ranged from −0.50 to −0.55 for toluene OH-/Cl-SOA, the higher H/C ratio observed for toluene OH-SOA was probably a consequence of OH addition to the aromatic ring for (at least) the first toluene + OH reaction step, given that the H/C ratio of toluene is 1.14. This pathway would initially increase the H/C ratio. Thereafter, addition of similar oxygen-containing functional groups to toluene OH-SOA and Cl-SOA over multiple oxidation steps resulted in similar reductions in H/C as a function of O/C. Similar trends were observed for isoprene and α-pinene OH-/Cl-SOA, with H/C offsets of approximately 0.15 (isoprene) and 0.07 (α-pinene) at a specific O/C ratio. Corresponding Van Krevelen slopes ranged from −0.55 to −0.60 for each OH- and Cl-SOA type. As with OH oxidation of toluene *via* direct addition, OH addition to double bond(s) present in isoprene and α-pinene would have also initially increased the H/C ratio relative to Cl-SOA generated from the same precursor. Here, the lower increase in H/C of isoprene OH-SOA relative to toluene OH-SOA suggests multiple OH additions to the toluene backbone occurred *via* ring-opening reactions. Subsequent addition of similar oxygen-containing functional groups by both OH and Cl oxidation would have then generated similar Van Krevelen slopes.

Whereas the O/C and H/C ratios of OH-SOA and Cl-SOA changed significantly as a function of OH$_{exp}$ or Cl$_{exp}$, changes in the elemental ratios of isoprene and α-pinene Br-SOA were relatively minor. The O/C and H/C ratios of isoprene Br-SOA ranged from 0.24 to 0.31 and 1.40 to 1.41, and O/C and H/C ratios of α-pinene Br-SOA ranged from 0.24 to 0.32 and 1.33 to 1.39. Along with Fig. 2f and l, Fig. 5 provides additional evidence that multistep oxidative aging of Br-SOA is less extensive than in OH-SOA and Cl-SOA.

3.5 OH-SOA, Cl-SOA, and Br-SOA mass yields

Fig. 6a–d shows mass yields of SOA as a function of OH$_{exp}$ and Cl$_{exp}$ for n-C$_{12}$, toluene, isoprene, and α-pinene. SOA yields obtained from Br oxidation of isoprene and α-pinene are also shown in Fig. 6c and d. Fig. S14† shows the same data that is plotted in Fig. 6, plus the corresponding SOA yield values without applying particle wall loss correction (pWLC) factors (Section 2.3.2). Results obtained from Cl oxidation of the same precursors in environmental chamber studies is provided in Table 3. Some of the environmental chamber α-pinene Cl-SOA yields, and all the n-C$_{12}$ Cl-SOA yields, were measured in the presence of added NO$_x$, whereas no NO$_x$ was added in OFR experiments. However, yields of n-C$_{12}$ OH-SOA do not display a systematic NO$_x$ dependence,[93] and it is not yet clear to what extent NO$_x$ affects α-pinene Cl-SOA yields.[29,31,36] Thus, to first order we assume NO$_x$ has less influence than other experimental variables such as oxidant type or Cl$_{exp}$ on yields of n-C$_{12}$ or α-pinene Cl-SOA.

Fig. 6a shows that yields of n-C$_{12}$ Cl-SOA and OH-SOA initially increased at lower Cl$_{exp}$ and OH$_{exp}$ following functionalization reactions that produced condensable LVOCs. At higher Cl$_{exp}$ and OH$_{exp}$, yields decreased due to fragmentation
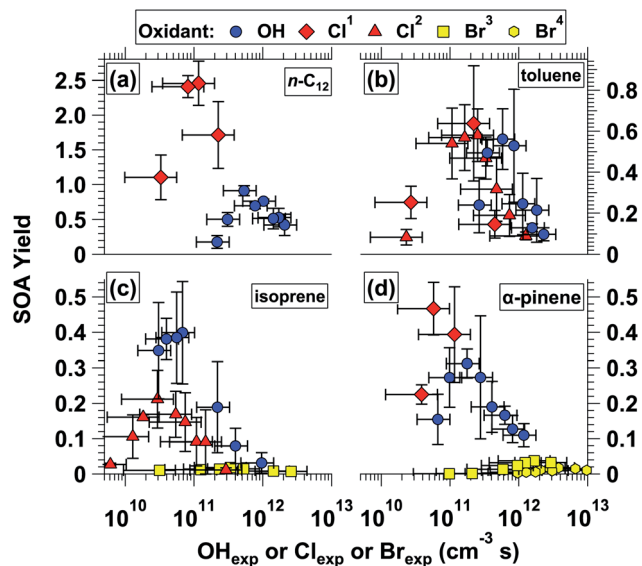
Fig. 6 Mass yields of SOA generated from (a) OH and Cl oxidation of n-C_{12}, (b) OH and Cl oxidation of toluene, (c) OH, Cl, and Br oxidation of isoprene, and (d) OH, Cl, and Br oxidation of α-pinene as a function of OH_{exp}, Cl_{exp}, or Br_{exp}. Different y-axis scales are used in each subpanel. Error bars indicate ±1σ uncertainty in binned SOA yield values, ±50% uncertainty in OH exposure values, and ±70% uncertainty in Cl and Br exposure values. Additional figure notes: [1]Cl generated using OFR254/313-iC$_2$Cl$_2$O$_2$; [2]Cl generated using OFR313/369-iCl$_2$; [3]Br generated using OFR254-iC$_2$Br$_2$O$_2$; [4]Br generated using OFR369/421-iBr$_2$.

reactions that generated higher-volatility oxidation products. Here, the observation that Cl-SOA yields exhibit similar trends as OH-SOA yields with increasing oxidation therefore builds on results obtained in previous OH-OFR laboratory and field studies.[23–28,78,94,95] For n-C_{12} Cl-SOA, the yield increased from 1.1 to 2.5 (0.92 to 1.9 without pWLC; Fig. S14†) as Cl_{exp} increased from 3.3×10^{10} to 8.2×10^{10} cm^{-3} s, then decreased to 1.7 (1.3 without pWLC) at $Cl_{exp} = 2.3 \times 10^{11}$ cm^{-3} s. For n-C_{12} OH-SOA, the yield increased from 0.18 to 0.91 (0.14 to 0.74 without pWLC) as OH_{exp} increased from 2.3×10^{11} to 5.4×10^{11} cm^{-3} s, then decreased to 0.42 (0.31 without pWLC) at $OH_{exp} = 2.1 \times 10^{12}$ cm^{-3} s. Thus, over the range of conditions shown in Fig. 6, the maximum n-C_{12} Cl-SOA yield was approximately 2.7 times higher than the maximum n-C_{12} OH-SOA yield. In chamber studies, n-C_{12} Cl-SOA yields ranged from 1.10 to 1.65 (ref. 33) ($Cl_{exp} = 9.8 \times 10^{10}$ to 1.3×10^{11} cm^{-3} s) and n-C_{12} OH-SOA yields ranged from 0.15 to 0.28 ($OH_{exp} = 2.2 \times 10^{11}$ to 4.3×10^{11} cm^{-3} s).[93]

Fig. 6b shows yields of toluene Cl-SOA and OH-SOA as a function of OH_{exp} and Cl_{exp}. Toluene Cl-SOA yields obtained *via* OFR254-iC$_2$Cl$_2$O$_2$ and OFR313/369-iCl$_2$ are represented by different symbols. At the lowest and highest Cl_{exp} values that were used (Table 1), Cl-SOA yields were 0.083 and 0.090, respectively. Maximum toluene Cl-SOA yields were 0.58 ± 0.13 at $Cl_{exp} = 2.5 \times 10^{11}$ cm^{-3} s *via* OFR313/369-iCl$_2$ and 0.64 ± 0.28 at $Cl_{exp} = 2.2 \times 10^{11}$ cm^{-3} *via* OFR254-iC$_2$Cl$_2$O$_2$. Toluene Cl-SOA yield values obtained in chambers ranged from 0.030 to 0.079 (ref. 30) and 0.33 to 0.67 (ref. 35) (Table 3). For toluene OH-SOA,

the yield increased from 0.24 to 0.56 as OH_{exp} increased from 2.6×10^{11} to 5.8×10^{11} cm^{-3} s, then decreased to 0.079 at $OH_{exp} = 2.3 \times 10^{12}$ cm^{-3} s. At the lowest OH_{exp} used here, our toluene OH-SOA yield value of 0.24 agrees within 14% of the toluene OH-SOA mass yield of 0.21 obtained at $OH_{exp} = 2.3 \times 10^{11}$ cm^{-3} by Hildebrandt Ruiz *et al.*[96] Overall, over the range of OFR conditions shown in Fig. 6b, Cl and OH oxidation of toluene generated maximum Cl-SOA and OH-SOA yield values that were within 14% of each other.

Fig. 6c shows yields of isoprene Cl-SOA, Br-SOA, and OH-SOA as a function of OH_{exp}, Cl_{exp}, and Br_{exp}. At the lowest and highest Cl_{exp} values shown in Fig. 6c, Cl-SOA yields were 0.027 and 0.011, respectively. The maximum isoprene Cl-SOA yield was 0.21 at $Cl_{exp} = 3.0 \times 10^{10}$ cm^{-3} s. By comparison, chamber isoprene Cl-SOA yield values ranged from 0.08 to 0.29.[32] The maximum isoprene Br-SOA yield was only 0.018 at $Br_{exp} = 3.8 \times 10^{11}$ cm^{-3} s, even when using a significantly higher isoprene mixing ratio than what was used in OH and Cl experiments (Table 1). The maximum isoprene OH-SOA yield measured here was 0.40 at $OH_{exp} = 6.8 \times 10^{10}$ cm^{-3} s, which was a higher yield than expected based on recent isoprene OH-SOA yield values measured in the absence of NO$_x$ in both OFRs (0.032 at $OH_{exp} = 7.8 \times 10^{11}$ cm^{-3} s (ref. 92)) and chambers (≤0.15 at $OH_{exp} \approx 5.1 \times 10^{10}$ cm^{-3} s (ref. 97)). Our results agree with those obtained by Lambe *et al.*[92] at comparable OH_{exp} because we observed an isoprene OH-SOA yield of 0.031 at $OH_{exp} = 9.6 \times 10^{11}$ cm^{-3} s. Thus, the lower OH_{exp} achieved in this study was a contributing factor to the higher OFR isoprene OH-SOA yield, presumably due to less fragmentation of the SOA. While $OH_{exp} = 6.8 \times 10^{10}$ cm^{-3} s is within ≈ 30% of the OH_{exp} we estimate was used by Liu *et al.*,[97] photochemical box modeling calculations suggest that mixing ratios of hydroperoxyl (HO$_2$) radicals were approximately 6 times higher in the OFR (≈3 ppb *vs.* 0.55 ppb). Because isoprene OH-SOA yields are sensitive to the rate of reaction between HO$_2$ and RO$_2$, we hypothesize that our results may have been obtained under conditions that favored HO$_2$ + RO$_2$ reactions to a greater extent, thereby leading to ≈2 times higher SOA yield values. Overall, over the range of OFR conditions shown in Fig. 6, Cl and Br oxidation of isoprene generated SOA with maximum yields that are 52% and 5% of those obtained *via* OH oxidation.

Fig. 6d shows yields of α-pinene Cl-SOA, Br-SOA and OH-SOA. As was done in isoprene Br-SOA studies, a higher α-pinene mixing ratio was used to generate enough mass of low-volatility oxidation products to promote homogenous nucleation of Br-SOA (Table 1). The maximum α-pinene Cl-SOA yield was 0.47 at $Cl_{exp} = 5.8 \times 10^{10}$ cm^{-3} s. Maximum α-pinene Br-SOA yields were 0.037 at $Br_{exp} = 1.7 \times 10^{12}$ cm^{-3} s (OFR254-iC$_2$Br$_2$O$_2$) and 0.018 at $Br_{exp} = (2.8–3.8) \times 10^{12}$ cm^{-3} s (OFR421-iBr$_2$). As summarized in Table 3, our α-pinene Cl-SOA yield values were within the range of chamber α-pinene Cl-SOA yield values between 0.079 to 0.22,[29] 0.11 to 0.62,[31] and 0.44 to 0.96.[36] For α-pinene OH-SOA, the maximum yield was 0.31 at $OH_{exp} = 1.8 \times 10^{11}$ cm^{-3} s, which is generally consistent with chamber α-pinene OH-SOA yield values obtained at comparable OH_{exp}.[98] Over the range of conditions shown in Fig. 6d, Cl and Br

© 2022 The Author(s). Published by the Royal Society of Chemistry

Environ. Sci.: Atmos., 2022, **2**, 687–701 | **697**

oxidation of α-pinene generates SOA at yields that are approximately 150% and 6–12% of those obtained *via* OH oxidation.

SOA photolysis at $\lambda = 254$ nm is a concern under certain OH-OFR conditions,[46] but direct experimental evaluation is difficult due to the lack of operable OH sources at longer photolysis wavelengths. Here, our measurements enable an investigation into the potential role of Cl-SOA and Br-SOA photolysis at $\lambda = 254$ nm through a comparison of the yields of toluene Cl-SOA generated *via* OFR254-iC$_2$Cl$_2$O$_2$ *versus* OFR313/369-iCl$_2$, and of α-pinene Br-SOA generated *via* OFR254-iC$_2$Br$_2$O$_2$ *versus* OFR369/421-iBr$_2$. If SOA photolysis at $\lambda = 254$ nm was significant, yields of toluene Cl-SOA and α-pinene Br-SOA obtained using OFR254-iC$_2$Cl$_2$O$_2$ and OFR254-iC$_2$Br$_2$O$_2$ would have been lower than those obtained *via* OFR313/369-iCl$_2$ and OFR369/421-iBr$_2$. This was not the case. For toluene Cl-SOA, in the three regions of approximate Cl$_{exp}$ overlap – $(2.3–2.7) \times 10^{10}$, $(2.2–2.5) \times 10^{11}$, and $(4.5–4.7) \times 10^{11}$ cm^{-3} s – toluene Cl-SOA yields obtained using OFR254-iC$_2$Cl$_2$O$_2$ were either higher than, or in agreement with, yields obtained using OFR313/369-iCl$_2$ within measurement uncertainties: 0.25 ± 0.08 *versus* 0.083 ± 0.038, 0.64 ± 0.28 *versus* 0.58 ± 0.13, and 0.15 ± 0.07 *versus* 0.32 ± 0.16, respectively. Similarly, α-pinene Br-SOA yields, obtained at Br$_{exp}$ ranging from 9.5×10^{11} to 2.9×10^{12} cm^{-3} s, were between 0.024 and 0.032 using OFR254-iC$_2$Br$_2$O$_2$, compared to 0.0028 to 0.017 when using OFR369/421-iBr$_2$. Thus, because halocarbons are typically photolabile, our results suggest that photolysis of Cl-SOA or Br-SOA was too slow to compete with multigenerational Cl- or Br-induced oxidative aging in the OFR. Because OH-SOA was also generated under conditions using $\lambda = 254$ nm radiation, and because OH-induced oxidative aging of SOA occurs to a similar or greater extent than Cl or Br, our results support previous modeling studies suggesting that OH-SOA measurements obtained using OFR185 are not significantly impacted by SOA photolysis at $\lambda = 254$ nm.[46]

4 Conclusions

In this study we characterized mass spectra, elemental ratios, and yields of SOA generated from the OH and Cl oxidation of representative anthropogenic precursors (*n*-C$_{12}$ and toluene) and the OH, Cl and Br oxidation of representative biogenic (isoprene and α-pinene) precursors. Overall, r^2-values between L-ToF-AMS spectra of Cl-SOA (and, where applicable, Br-SOA) and OH-SOA generated from the same precursor ranged from 0.57 to 0.94 at low oxidant exposures (Fig. 1a–d and 2a–f). The highest r^2-value was observed between *n*-C$_{12}$ OH- and Cl-SOA spectra, which was expected because OH- and Cl-induced oxidative aging occurred primarily *via* hydrogen atom abstraction. Van Krevelen diagrams of *n*-C$_{12}$ OH- and Cl-SOA also had the highest degree of similarity (Fig. 5a). In cases where OH, Cl, and/or Br addition to unsaturated precursors (toluene, isoprene, α-pinene) was possible, the r^2 values between Cl-/Br-SOA and OH-SOA were lower, and the H/C ratios of Cl-/Br-SOA were systematically lower than H/C ratios of OH-SOA (Fig. 5b–d). Additionally, the presence of C$_x$H$_y$ClO$_z^+$ and C$_x$H$_y$BrO$_z^+$ ions in Cl-SOA and Br-SOA were clear indicators of halogen-initiated oxidative aging that may be used to investigate Cl- and Br-induced oxidative aging signatures in

ambient AMS datasets. Across the full range of oxidant exposures that were studied, fundamental differences between Br- and OH-/Cl-initiated oxidative aging pathways were evident; namely, that multistep SOA oxidative aging is significant when initiated by OH and Cl, but not by Br.

Our SOA yield measurements indicate that specific precursors generated SOA at yields that were strongly dependent on the oxidant and exposure time. Across all OFR conditions that were used, OH oxidation of *n*-C$_{12}$, toluene, isoprene and α-pinene resulted in maximum OH-SOA yields ranging from 0.31 to 0.91; Cl oxidation of the same precursors, at the same precursor mixing ratios, generated Cl-SOA at maximum yields ranging from 0.21 to 2.5. Br oxidation of isoprene and α-pinene generated Br-SOA at maximum yields ranging from 0.018 to 0.037, suggesting that multigenerational oxidative aging may be required to achieve the range of yield values obtained across the OH-SOA and Cl-SOA systems examined here.

Notably, even though *n*-C$_{12}$ OH-SOA and Cl-SOA had the highest degree of similarity in chemical composition, maximum *n*-C$_{12}$ Cl-SOA and OH-SOA yields were the most different: the yield of *n*-C$_{12}$ Cl-SOA was 2.7 times higher than the corresponding maximum *n*-C$_{12}$ OH-SOA yield. This may be due to Cl preferentially reacting with terminal carbons on the *n*-C$_{12}$ backbone,[99] which could provide a longer effective carbon chain length for peroxy radicals to undergo intramolecular hydrogen shift reactions leading to SOA formation *via* autooxidation.[100] Because OH reacts with both terminal and non-terminal carbons with similar probability, this may have resulted in more *n*-C$_{12}$ OH-SOA fragmentation relative to *n*-C$_{12}$ Cl-SOA.[99] On the other hand, while toluene OH-SOA and Cl-SOA had the lowest degree of chemical similarity, maximum toluene OH-SOA and Cl-SOA mass yields were the closest in value. Overall, our results suggest that alkane, aromatic, and terpenoid SOA precursors are characterized by distinct OH- and halogen-initiated SOA yields, and that while Cl may enhance the SOA formation potential in regions influenced by biogenic and anthropogenic emissions, Br may have the opposite effect. Characterizing the molecular composition of specific oxidation products that contribute to OH-, Cl- and Br-SOA formation, and expanding the photochemical model introduced in Section 2.1.3 to include VOC + Cl/Br oxidation chemistry, may provide further insight into the trends observed here and will be the focus of future work.

Author contributions

AL conceived and planned the experiments. AL and AA carried out the OFR experiments and performed data analysis. DW and CM provided unpublished data from previous chamber Cl-SOA experiments, and MM calculated Cl exposure values in those chamber Cl-SOA experiments. AL, AA, NB, LHR, and WHB contributed to the interpretation of the results. AL took the lead in writing the manuscript. All authors provided feedback on the manuscript.

Conflicts of interest

There are no conflicts to declare.

Acknowledgements

References

1 B. J. Finlayson-Pitts and J. N. Pitts Jr, *Chemistry of the Upper and Lower Atmosphere: Theory, Experiments, and Applications*, Academic Press, 2000.

2 R. P. Wayne, I. Barnes, P. Biggs, J. P. Burrows, C. E. Canosa-Mas, J. Hjorth, G. Le Bras, G. K. Moortgat, D. Perner, G. Poulet, G. Restelli and H. Sidebottom, *Atmos. Environ., Part A*, 1991, **25**, 1–203.

3 S. S. Brown, H. D. Osthoff, H. Stark, W. P. Dubé, T. B. Ryerson, C. Warneke, J. A. de Gouw, A. G. Wollny, D. D. Parrish, F. C. Fehsenfeld and A. Ravishankara, *J. Photochem. Photobiol., A*, 2005, **176**, 270–278.

4 Z. C. J. Decker, M. A. Robinson, K. C. Barsanti, I. Bourgeois, M. M. Coggon, J. P. DiGangi, G. S. Diskin, F. M. Flocke, A. Franchin, C. D. Fredrickson, G. I. Gkatzelis, S. R. Hall, H. Halliday, C. D. Holmes, L. G. Huey, Y. R. Lee, J. Lindaas, A. M. Middlebrook, D. D. Montzka, R. Moore, J. A. Neuman, J. B. Nowak, B. B. Palm, J. Peischl, F. Piel, P. S. Rickly, A. W. Rollins, T. B. Ryerson, R. H. Schwantes, K. Sekimoto, L. Thornhill, J. A. Thornton, G. S. Tyndall, K. Ullmann, P. Van Rooy, P. R. Veres, C. Warneke, R. A. Washenfelder, A. J. Weinheimer, E. Wiggins, E. Winstead, A. Wisthaler, C. Womack and S. S. Brown, *Atmos. Chem. Phys.*, 2021, **21**, 16293–16317.

5 N. L. Ng, S. S. Brown, A. T. Archibald, E. Atlas, R. C. Cohen, J. N. Crowley, D. A. Day, N. M. Donahue, J. L. Fry, H. Fuchs, R. J. Griffin, M. I. Guzman, H. Herrmann, A. Hodzic, Y. Iinuma, J. L. Jimenez, A. Kiendler-Scharr, B. H. Lee, D. J. Luecken, J. Mao, R. McLaren, A. Mutzel, H. D. Osthoff, B. Ouyang, B. Picquet-Varrault, U. Platt, H. O. T. Pye, Y. Rudich, R. H. Schwantes, M. Shiraiwa, J. Stutz, J. A. Thornton, A. Tilgner, B. J. Williams and R. A. Zaveri, *Atmos. Chem. Phys.*, 2017, **17**, 2103–2162.

6 O. W. Wingenter, M. K. Kubo, N. J. Blake, T. W. Smith Jr, D. R. Blake and F. S. Rowland, *J. Geophys. Res.*, 1996, **101**, 4331–4340.

7 A. K. Baker, C. Sauvage, U. R. Thorenz, P. van Velthoven, D. E. Oram, A. Zahn, C. A. M. Brenninkmeijer and J. Williams, *Sci. Rep.*, 2016, **6**, 36821.

8 J. Liao, L. G. Huey, Z. Liu, D. J. Tanner, C. A. Cantrell, J. J. Orlando, F. M. Flocke, P. B. Shepson, A. J. Weinheimer, S. R. Hall, K. Ullmann, H. J. Beine, Y. Wang, E. D. Ingall, C. R. Stephens, R. S. Hornbrook,

E. C. Apel, D. Riemer, A. Fried, R. L. Mauldin III, J. N. Smith, R. M. Staebler, J. A. Neuman and J. B. Nowak, *Nat. Geosci.*, 2014, **7**, 91.

9 K. A. Pratt, *Trends Chem.*, 2019, **1**, 545–548.

10 T. P. Riedel, N. L. Wagner, W. P. Dubé, A. M. Middlebrook, C. J. Young, F. Öztürk, R. Bahreini, T. C. VandenBoer, D. E. Wolfe, E. J. Williams, J. M. Roberts, S. S. Brown and J. A. Thornton, *J. Geophys. Res.: Atmos.*, 2013, **118**, 8702–8715.

11 C. B. Faxon, J. K. Bean and L. Hildebrandt Ruiz, *Atmosphere*, 2015, **6**, 1487–1506.

12 M. Priestley, M. le Breton, T. J. Bannan, S. D. Worrall, A. Bacak, A. R. D. Smedley, E. Reyes-Villegas, A. Mehra, J. Allan, A. R. Webb, D. E. Shallcross, H. Coe and C. J. Percival, *Atmos. Chem. Phys.*, 2018, **18**, 13481–13493.

13 J. P. S. Wong, N. Carslaw, R. Zhao, S. Zhou and J. P. D. Abbatt, *Indoor Air*, 2017, **27**, 1082–1090.

14 H. Schwartz-Narbonne, C. Wang, S. Zhou, J. P. Abbatt and J. Faust, *Environ. Sci. Technol.*, 2019, **53**, 1217–1224.

15 J. M. Mattila, P. S. J. Lakey, M. Shiraiwa, C. Wang, J. P. D. Abbatt, C. Arata, A. H. Goldstein, L. Ampollini, E. F. Katz, P. F. DeCarlo, S. Zhou, T. F. Kahan, F. J. Cardoso-Saldaña, L. H. Ruiz, A. Abeleira, E. K. Boedicker, M. E. Vance and D. K. Farmer, *Environ. Sci. Technol.*, 2020, **54**, 1730–1739.

16 Q. Li, X. Fu, X. Peng, W. Wang, A. Badia, R. P. Fernandez, C. A. Cuevas, Y. Mu, J. Chen, J. L. Jimenez, T. Wang and A. Saiz-Lopez, *Environ. Sci. Technol.*, 2021, **55**, 13625–13637.

17 L. A. Barrie, J. W. Bottenheim, R. C. Schnell, P. J. Crutzen and R. A. Rasmussen, *Nature*, 1988, **334**, 138–141.

18 C. R. Stephens, P. B. Shepson, A. Steffen, J. W. Bottenheim, J. Liao, L. G. Huey, E. Apel, A. Weinheimer, S. R. Hall, C. Cantrell, B. C. Sive, D. J. Knapp, D. D. Montzka and R. S. Hornbrook, *J. Geophys. Res.*, 2012, **117**, D00R11.

19 T. Moise and Y. Rudich, *Geophys. Res. Lett.*, 2001, **28**, 4083–4086.

20 J. Ofner, N. Balzer, J. Buxmann, H. Grothe, P. Schmitt-Kopplin, U. Platt and C. Zetzsch, *Atmos. Chem. Phys.*, 2012, **12**, 5787–5806.

21 J. Buxmann, S. Bleicher, U. Platt, R. von Glasow, R. Sommariva, A. Held, C. Zetzsch and J. Ofner, *Environ. Chem.*, 2015, **12**, 476–488.

22 T. B. Nguyen, J. D. Crounse, R. H. Schwantes, A. P. Teng, K. H. Bates, X. Zhang, J. M. St. Clair, W. H. Brune, G. S. Tyndall, F. N. Keutsch, J. H. Seinfeld and P. O. Wennberg, *Atmos. Chem. Phys.*, 2014, **14**, 13531–13549.

23 A. T. Lambe, T. B. Onasch, D. R. Croasdale, J. P. Wright, A. T. Martin, J. P. Franklin, P. Massoli, J. H. Kroll, M. R. Canagaratna, W. H. Brune, D. R. Worsnop and P. Davidovits, *Environ. Sci. Technol.*, 2012, **46**, 5430–5437.

24 D. S. Tkacik, A. T. Lambe, S. Jathar, X. Li, A. A. Presto, Y. Zhao, D. Blake, S. Meinardi, J. T. Jayne, P. L. Croteau and A. L. Robinson, *Environ. Sci. Technol.*, 2014, **48**, 11235–11242.

25 A. M. Ortega, P. L. Hayes, Z. Peng, B. B. Palm, W. Hu, D. A. Day, R. Li, M. J. Cubison, W. H. Brune, M. Graus, C. Warneke, J. B. Gilman, W. C. Kuster, J. De Gouw,

© 2022 The Author(s). Published by the Royal Society of Chemistry

Environ. Sci.: Atmos., 2022, **2**, 687–701 | **699**

C. Gutiérrez-Montes and J. L. Jimenez, *Atmos. Chem. Phys.*, 2016, **16**, 7411–7433.

26 B. A. Nault, P. Campuzano-Jost, D. A. Day, J. C. Schroder, B. Anderson, A. J. Beyersdorf, D. R. Blake, W. H. Brune, Y. Choi, C. A. Corr, J. A. de Gouw, J. Dibb, J. P. DiGangi, G. S. Diskin, A. Fried, L. G. Huey, M. J. Kim, C. J. Knote, K. D. Lamb, T. Lee, T. Park, S. E. Pusede, E. Scheuer, K. L. Thornhill, J.-H. Woo and J. L. Jimenez, *Atmos. Chem. Phys.*, 2018, **18**, 17769–17800.

27 W. Hu, H. Zhou, W. Chen, Y. Ye, T. Pan, Y. Wang, W. Song, H. Zhang, W. Deng, M. Zhu, C. Wang, C. Wu, C. Ye, Z. Wang, B. Yuan, S. Huang, M. Shao, Z. Peng, D. A. Day, P. Campuzano-Jost, A. T. Lambe, D. R. Worsnop, J. L. Jimenez and X. Wang, *Environ. Sci. Technol.*, 2021, DOI: 10.1021/acs.est.1c03155.

28 K. Liao, Q. Chen, Y. Liu, Y. J. Li, A. T. Lambe, T. Zhu, R.-J. Huang, Y. Zheng, X. Cheng, R. Miao, G. Huang, R. B. Khuzestani and T. Jia, *Environ. Sci. Technol.*, 2021, **55**(11), 7276–7286.

29 X. Cai and R. J. Griffin, *J. Geophys. Res.*, 2006, **111**, D14206.

30 X. Cai, L. D. Ziemba and R. J. Griffin, *Atmos. Environ.*, 2008, **42**, 7348–7359.

31 J. Ofner, K. A. Kamilli, A. Held, B. Lendl and C. Zetzsch, *Faraday Discuss.*, 2013, **165**, 135–149.

32 D. S. Wang and L. Hildebrandt Ruiz, *Atmos. Chem. Phys.*, 2017, **17**, 13491–13508.

33 D. S. Wang and L. Hildebrandt Ruiz, *Atmos. Chem. Phys.*, 2018, **18**, 15535–15553.

34 Y. Wang, M. Riva, H. Xie, L. Heikkinen, S. Schallhart, Q. Zha, C. Yan, X.-C. He, O. Peräkylä and M. Ehn, *Atmos. Chem. Phys.*, 2020, **20**, 5145–5155.

35 S. V. Dhulipala, S. Bhandari and L. Hildebrandt Ruiz, *Atmos. Environ.*, 2019, **199**, 265–273.

36 C. G. Masoud and L. Hildebrandt Ruiz, *ACS Earth Space Chem.*, 2021, **5**, 2307–2319.

37 J. D. Crounse, L. B. Nielsen, S. Jørgensen, H. G. Kjaergaard and P. O. Wennberg, *J. Phys. Chem. Lett.*, 2013, **4**, 3513–3520.

38 H. Zhang, D. R. Worton, S. Shen, T. Nah, G. Isaacman-VanWertz, K. R. Wilson and A. H. Goldstein, *Environ. Sci. Technol.*, 2015, **49**, 9768–9777.

39 J. P. Rowe, A. T. Lambe and W. H. Brune, *Atmos. Chem. Phys.*, 2020, **20**, 13417–13424.

40 B. L. Deming, D. Pagonis, X. Liu, D. A. Day, R. Talukdar, J. E. Krechmer, J. A. de Gouw, J. L. Jimenez and P. J. Ziemann, *Atmos. Meas. Tech.*, 2019, **12**, 3453–3461.

41 A. T. Lambe, J. E. Krechmer, Z. Peng, J. R. Casar, A. J. Carrasquillo, J. D. Raff, J. L. Jimenez and D. R. Worsnop, *Atmos. Meas. Tech.*, 2019, **12**, 299–311.

42 J. Mao, X. Ren, W. Brune, J. Olson, J. Crawford, A. Fried, L. Huey, R. Cohen, B. Heikes and H. Singh, *Atmos. Chem. Phys.*, 2009, **9**, 163–173.

43 A. V. Baklanov and L. N. Krasnoperov, *J. Phys. Chem. A*, 2001, **105**, 97–103.

44 B. Ghosh, D. K. Papanastasiou and J. B. Burkholder, *J. Chem. Phys.*, 2012, **137**, 164315.

45 M. Riva, R. M. Healy, P.-M. Flaud, E. Perraudin, J. C. Wenger and E. Villenave, *J. Phys. Chem. A*, 2015, **119**, 11170–11181.

46 Z. Peng, D. A. Day, A. M. Ortega, B. B. Palm, W. Hu, H. Stark, R. Li, K. Tsigaridis, W. H. Brune and J. L. Jimenez, *Atmos. Chem. Phys.*, 2016, **16**, 4283–4305.

47 C.-C. Wu, H.-C. Lin, Y.-B. Chang, P.-Y. Tsai, Y.-Y. Yeh, H. Fan, K.-C. Lin and J. S. Francisco, *J. Chem. Phys.*, 2011, **135**, 234308.

48 D. Paul, H. K. Kim, M. M. Rahman and T. K. Kim, *J. Appl. Spectrosc.*, 2021, **88**, 737–743.

49 D. Maric, J. Burrows, R. Meller and G. Moortgat, *J. Photochem. Photobiol., A*, 1993, **70**, 205–214.

50 D. Maric, J. Burrows and G. Moortgat, *J. Photochem. Photobiol., A*, 1994, **83**, 179–192.

51 J. E. Tuttle and G. K. Rollefson, *J. Am. Chem. Soc.*, 1941, **63**, 1525–1530.

52 H. Shimada, R. Shimada and Y. Kanda, *Bull. Chem. Soc. Jpn.*, 1968, **41**, 1289–1295.

53 R. Atkinson, D. L. Baulch, R. A. Cox, J. N. Crowley, R. F. Hampson, R. G. Hynes, M. E. Jenkin, M. J. Rossi and J. Troe, *Atmos. Chem. Phys.*, 2007, 7, 981–1191.

54 Z. Peng and J. L. Jimenez, *J. Chem. Educ.*, 2019, **96**, 806–811.

55 R. Li, B. B. Palm, A. M. Ortega, J. Hlywiak, W. Hu, Z. Peng, D. A. Day, C. Knote, W. H. Brune, J. A. De Gouw and J. L. Jimenez, *J. Phys. Chem. A*, 2015, **119**, 150406123535006.

56 Z. Peng and J. L. Jimenez, *Chem. Soc. Rev.*, 2020, **49**, 2570–2616.

57 P. F. Liu, N. Abdelmalki, H.-M. Hung, Y. Wang, W. H. Brune and S. T. Martin, *Atmos. Chem. Phys.*, 2015, **15**, 1435–1446.

58 P. Campuzano-Jost, B. Nault, T. Koenig, H. Guo, J. Schroder, D. Day, J. Jimenez, R. Volkamer, K. Froyd, D. Murphy, A. Kupc, C. Williamson and C. Brock, in *18th AMS Users Meeting*, 2018.

59 L. Jaegle, Y. C. Chan, D. Kim, P. Campuzano-Jost and J. L. Jimenez, *AGU Fall Meeting*, 2021.

60 S. M. Pieber, I. El Haddad, J. G. Slowik, M. R. Canagaratna, J. T. Jayne, S. M. Platt, C. Bozzetti, K. R. Daellenbach, R. Fröhlich, A. Vlachou, F. Klein, J. Dommen, B. Miljevic, J. L. Jiménez, D. R. Worsnop, U. Baltensperger and A. S. H. Prévôt, *Environ. Sci. Technol.*, 2016, **50**, 10494–10503.

61 B. Rao, T. A. Anderson, A. Redder and W. A. Jackson, *Environ. Sci. Technol.*, 2010, **44**, 2961–2967.

62 L. Jaeglé, Y. L. Yung, G. C. Toon, B. Sen and J.-F. Blavier, *Geophys. Res. Lett.*, 1996, **23**, 1749–1752.

63 D. Sueper, 2022, https://cires.colorado.edu/jimenez-group/ToFAMSResources/ToFSoftware.

64 A. C. Aiken, P. F. DeCarlo, J. H. Kroll, D. R. Worsnop, J. A. Huffman, K. S. Docherty, I. M. Ulbrich, C. Mohr, J. R. Kimmel and D. Sueper, *Environ. Sci. Technol.*, 2008, **42**, 4478–4485.

65 P. S. Chhabra, N. L. Ng, M. R. Canagaratna, A. L. Corrigan, L. M. Russell, D. R. Worsnop, R. C. Flagan and J. H. Seinfeld, *Atmos. Chem. Phys.*, 2011, **11**, 8827–8845.

66 L. D. Yee, J. S. Craven, C. L. Loza, K. A. Schilling, N. L. Ng, M. R. Canagaratna, P. J. Ziemann, R. C. Flagan and J. H. Seinfeld, *J. Phys. Chem. A*, 2012, **116**, 6211–6230.

67 M. R. Canagaratna, J. L. Jimenez, J. H. Kroll, Q. Chen, S. H. Kessler, P. Massoli, L. Hildebrandt Ruiz, E. Fortner, L. R. Williams and K. R. Wilson, *Atmos. Chem. Phys.*, 2015, **15**, 253–272.

68 N. L. Ng, M. R. Canagaratna, J. L. Jimenez, P. S. Chhabra, J. H. Seinfeld and D. R. Worsnop, *Atmos. Chem. Phys.*, 2011, **11**, 6465–6474.

69 M. Kuwata, W. Shao, R. Lebouteiller and S. T. Martin, *Atmos. Chem. Phys.*, 2013, **13**, 5309–5324.

70 R. Atkinson, *Chem. Rev.*, 1986, **86**, 69–201.

71 R. Atkinson, *Atmos. Chem. Phys.*, 2003, **3**, 2233–2307.

72 A. Bierbach, I. Barnes and K. H. Becker, *Int. J. Chem. Kinet.*, 1996, **28**, 565–577.

73 J. J. Orlando, G. S. Tyndall, E. C. Apel, D. D. Riemer and S. E. Paulson, *Int. J. Chem. Kinet.*, 2003, **35**, 334–353.

74 L. Renbaum-Wolff and G. D. Smith, *J. Phys. Chem. A*, 2012, **116**, 6664–6674.

75 J. Shi and M. J. Bernhard, *Int. J. Chem. Kinet.*, 1997, **29**, 349–358.

76 B. Shi, W. Wang, L. Zhou, Z. Sun, C. Fan, Y. Chen, W. Zhang, Y. Qiao, Y. Qiao and M. Ge, *Atmos. Environ.*, 2020, **222**, 117166.

77 C. Bhattarai, V. Samburova, D. Sengupta, M. Iaukea-Lum, A. C. Watts, H. Moosmüller and A. Y. Khlystov, *Aerosol Sci. Technol.*, 2018, **52**, 1266–1282.

78 B. B. Palm, P. Campuzano-Jost, A. M. Ortega, D. A. Day, L. Kaser, W. Jud, T. Karl, A. Hansel, J. F. Hunter, E. S. Cross, J. H. Kroll, Z. Peng, W. H. Brune and J. L. Jimenez, *Atmos. Chem. Phys.*, 2016, **16**, 2943–2970.

79 A. T. Lambe and J. L. Jimenez, *PAM Wiki*, https://sites.google.com/site/pamwiki/estimation-equations?authuser=0.

80 M. Dal Maso, M. Kulmala, K. E. J. Lehtinen, J. M. Mäkelä, P. Aalto and C. D. O'Dowd, *J. Geophys. Res.: Atmos.*, 2002, **107**, PAR 2.

81 A. T. Lambe, M. A. Miracolo, C. J. Hennigan, A. L. Robinson and N. M. Donahue, *Environ. Sci. Technol.*, 2009, **43**, 8794–8800.

82 W. H. Brune, *Environ. Sci. Technol.*, 2019, **53**, 3645–3652.

83 Y. He, A. T. Lambe, J. H. Seinfeld, C. D. Cappa, J. R. Pierce and S. H. Jathar, *Environ. Sci. Technol.*, 2022, DOI: 10.1021/acs.est.1c08520, Article ASAP.

84 N. Takegawa, T. Miyakawa, K. Kawamura and Y. Kondo, *Aerosol Sci. Technol.*, 2007, **41**, 418–437.

85 M. M. Maricq, J. J. Szente, E. W. Kaiser and J. Shi, *J. Phys. Chem.*, 1994, **98**, 2083–2089.

86 R. Atkinson, D. L. Baulch, R. A. Cox, J. N. Crowley, R. F. Hampson Jr, J. A. Kerr, M. J. Rossi, J. Troe, *IUPAC Subcommittee on Gas Kinetic Data Evaluation for Atmospheric Chemistry - Web Version*, 2001.

87 J. S. Francisco and J. N. Crowley, *J. Phys. Chem. A*, 2006, **110**, 3778–3784.

88 S. Enami, T. Yamanaka, T. Nakayama, S. Hashimoto, M. Kawasaki, D. E. Shallcross, Y. Nakano and T. Ishiwata, *J. Phys. Chem. A*, 2007, **111**, 3342–3348.

89 J. A. Manion, R. E. Huie, R. D. Levin, D. R. B. Burgess Jr, V. L. Orkin, W. Tsang, W. S. McGivern, J. W. Hudgens, V. D. Knyazev, D. B. Atkinson, E. Chai, A. M. Tereza, C.-Y. Lin, T. C. Allison, W. G. Mallard, F. Westley, J. T. Herron, R. F. Hampson and D. H. Frizzell, *NIST Chemical Kinetics Database, NIST Standard Reference Database 17, Version 7.0 (Web Version), Release 1.6.8, Data version 2015.09*, National Institute of Standards and Technology technical report, 2015.

90 C. L. Heald, J. H. Kroll, J. L. Jimenez, K. S. Docherty, P. F. Decarlo, A. C. Aiken, Q. Chen, S. T. Martin, D. K. Farmer and P. Artaxo, *Geophys. Res. Lett.*, 2010, **37**, L08803.

91 E. A. Bruns, I. El Haddad, -A. Keller, F. Klein, N. K. Kumar, S. M. Pieber, J. C. Corbin, J. G. Slowik, W. H. Brune, U. Baltensperger and A. S. H. Prevot, *Atmos. Meas. Tech.*, 2015, **8**, 2315–2332.

92 A. T. Lambe, P. S. Chhabra, T. B. Onasch, W. H. Brune, J. F. Hunter, J. H. Kroll, M. J. Cummings, J. F. Brogan, Y. Parmar, D. R. Worsnop, C. E. Kolb and P. Davidovits, *Atmos. Chem. Phys.*, 2015, **15**, 3063–3075.

93 C. L. Loza, J. S. Craven, L. D. Yee, M. M. Coggon, R. H. Schwantes, M. Shiraiwa, X. Zhang, K. A. Schilling, N. L. Ng, M. R. Canagaratna, P. J. Ziemann, R. C. Flagan and J. H. Seinfeld, *Atmos. Chem. Phys.*, 2014, **14**, 1423–1439.

94 K. Li, J. Liggio, P. Lee, C. Han, Q. Liu and S.-M. Li, *Atmos. Chem. Phys.*, 2019, **19**, 9715–9731.

95 W. Xu, Z. Li, A. T. Lambe, J. Li, T. Liu, A. Du, Z. Zhang, W. Zhou and Y. Sun, *Environ. Res.*, 2022, **209**, 112751.

96 L. Hildebrandt Ruiz, A. L. Paciga, K. M. Cerully, A. Nenes, N. M. Donahue and S. N. Pandis, *Atmos. Chem. Phys.*, 2015, **15**, 8301–8313.

97 J. Liu, E. L. D'Ambro, B. H. Lee, F. D. Lopez-Hilfiker, R. A. Zaveri, J. C. Rivera-Rios, F. N. Keutsch, S. Iyer, T. Kurten, Z. Zhang, A. Gold, J. D. Surratt, J. E. Shilling and J. A. Thornton, *Environ. Sci. Technol.*, 2016, **50**, 9872–9880.

98 N. C. Eddingsaas, C. L. Loza, L. D. Yee, M. Chan, K. A. Schilling, P. S. Chhabra, J. H. Seinfeld and P. O. Wennberg, *Atmos. Chem. Phys.*, 2012, **12**, 7413–7427.

99 L. G. Jahn, D. S. Wang, S. V. Dhulipala and L. Hildebrandt Ruiz, *J. Phys. Chem. A*, 2021, **125**, 7303–7317.

100 T. F. Mentel, M. Springer, M. Ehn, E. Kleist, I. Pullinen, T. Kurtén, M. Rissanen, A. Wahner and J. Wildt, *Atmos. Chem. Phys.*, 2015, **15**, 6745–6765.

© 2022 The Author(s). Published by the Royal Society of Chemistry

Environ. Sci.: Atmos., 2022, **2**, 687–701 | **701**